In vivo selective detection of highly polarized spin using MR

Ryuji Igarashi

Department of Molecular Engineering,

Graduate School of Engineering, Kyoto University

2012

Acknowledgments

These works were performed under the direction of Professor Masahiro Shirakawa. I would like to express my graduate for his guidance and discussion throughout these works. I also thank him for providing me a comfortable working environment and am proud of the challenge to these themes. I wish to express his sincere gratitude to Associate Professors Hidehito Tochio and Mariko Ariyoshi for their guidance and constructive discussions through the course of these studies. I also wish to express my sincere appreciations to Assistant Professor Kyohei Arita for his help and advice.

It should be emphasized that the studies in this thesis have required the cooperation with a number of groups of investigation. I wish to express my gratitude to Professor Yasuhiro Aoyama (Department of Molecular Chemistry and Biochemistry, Doshisha University) and Professor Shinsuke Sando (INAMORI Frontier Research Center, Kyushu University) for the wonderful conception that the signals of stable isotope-labeled biomolecules/metabolites can be selectively

Turned ON/OFF using triple resonance NMR. I wish thank to Dr Tomomi Sakai (Mitsubishi Kagaku Institute of Life Sciences) and Assistant Professor Takeshi Tenno (Department of Biological Science, Nagoya University) for instruction about preparation and microinjection of spin-labeled proteins, and also thank to Dr Hideyuki Hara (Bruker Biospin K.K.) for their support in Pulsed ESR measurements. I gratefully thank Professor Yoshie Harada, Associate Professor Yosuke Yoshinari and Senior Lecturer Hiroaki Yokota (Institute for Integrated Cell-Material Sciences, Kyoto University) for their helps and discussions in ODMR microscopy.

March, 2012

Kyoto Japan

Ryuji Igarashi

List of publications

Chapter 2

Turn-on detection of targeted biochemical reactions by triple resonance NMR analysis using isotope-labeled probe

Keigo Mizusawa*, Ryuji Igarashi*, Kosei Uehira, Yoshimasa Takafuji, Yasuhiko Tabata, Hidehito Tochio, Masahiro Shirakawa, Shinsuke Sando and Yasuhiro Aoyama

(*K. Mizusawa and R. Igarashi equally contributed to this work.)

Chem. Lett., **2010**, 39(9), pp926-928

Chapter 3

Distance Determination in Proteins inside Xenopus laevis Oocytes by Double Electron-Electron Resonance Experiments

Ryuji Igarashi, Tomomi Sakai, Hideyuki Hara, Takeshi Tenno, Toshiaki Tanaka, Hidehito Tochio and Masahiro Shirakawa

J. Am. Chem. Soc., **2010**, 132 (24), pp 8228–8229

Chapter 4

Real-time background-free selective imaging and orientation tracking of fluorescent nanodimamonds in vivo

Ryuji Igarashi, Hiroaki Yokota, Takuma Sugi, Kazuhiro Ikeda, Hitoshi Sumiya, Shigenori Tsuji, Ikue Mori, Hidehito Tochio, Yohsuke Yoshinari, Yoshie Harada, Masahiro Shirakawa

Manuscript in preparation

Contents

Chapter 1

General introduction

1.1 Significance of *in vivo* selective measurement

The brilliant successes of molecular biology in the twentieth century were derived from the adoption of the reductionistic paradigm shift made possible by the minimization of the complexity of life. Researchers in molecular biology, including myself, separate notable molecules from the biosystem, study the structures and functions and reconstruct a simplified fragment of the pluralist system to make a hypothetic model. And then we spend a significant amount of time finding sign which link *in vitro* information to *in vivo* measurement.

Several modalities have been utilized for non-invasive *in vivo* measurement such as ultrasound, X-ray computed tomography, scintigraphic, magnetic resonance (MR), and optics.[1-6] Of all these modalities, Only MR can also be used to obtain high-resolution structural information of molecules. *In vivo* MR measurement offers much information of living system mainly using ^{1}H MR principle. However, the detection of molecules of interest is often difficult because of spectral overlaps with a large number of intrinsic biomolecules. Although stable isotope labeling such as Carbon-13 or Nitrogen-15 is often used to detect target molecules selectively[7], direct ^{13}C or ^{15}N MR measurements *in vivo* are not often used due to the small thermal Boltzmann polarization and thus low sensitivity. Primary limitation of *in vivo* MR selective measurement using stable isotope labeling is the sensitivity, requiring high concentrations of no less than 0.1 mM.

1.2 Triple Resonance NMR

The intensity of a magnetic resonance signal is directly proportional to the population of the energy levels of the nuclei in a given magnetic field. Primary limitation of stable isotope-labeling is the intrinsically poor sensitivity due to the small thermal Boltzmann polarization. Even so, stable isotope labeling for *in vivo* MR measurement is one of the most promising techniques for the *in vivo* analysis of biochemical events. Multiple-resonance NMR is coherent magnetization transfer technique through j-coupling. We can use this technique to detect ^{13}C or ^{15}N labeled molecules indirectly by observation of much stronger proton signal.[8]

However, the detection of target molecules or reactions of interest is often difficult *in vivo* because of spectral overlaps with a large number of intermediates/metabolites themselves. NMR-active isotope-labeled molecules and their intermediates/metabolites are highly potential probes in principle. These probes and derived various intermediates/metabolites all serve as possible origins of background noise signals, and thus target metabolite should be carefully discriminated from others by the precise analysis of the chemical shifts. In this context, ideal chemical probes are those with a signal on/off device, that are otherwise NMR-silent and is rendered NMR-active only when accumulated at target sites and subjected to specific biochemical events.[2-20]

In Chapter 2, I report the feasibility of triple resonance NMR technique for the detection of isotopically labeled metabolites generated in cells and in injected mice with

higher selectivity of ^{1}H, the most sensitive and thus attractive nucleus. In addition, for the first time, we report on a signal-activatable glucose-based probe, which turns "on" its ^{1}H NMR signals as a result of target anaerobic glycolytic reaction.

1.3 Site-Directed Spin Labeling and Double Electron-Electron Resonance

We can also use higher thermal Boltzmann polarization of Electron spin instead of small polarization of nuclear spin. Pulsed ESR techniques, such combined with site-directed spin labeling (SDSL), are receiving increasing attention in structural biology because they provide a means for accurate determination of relatively long distances between electron spin centers introduced into proteins of interest.[21,22] With these methods, distributions of interspin distances of SDSL proteins in a range from 1.5 to 8 nm have been reported. This broad range of measurable distances is comparable to that of the FRET (Förster Resonance Energy Transfer) technique, but because the spin-label probes are smaller than the fluorophores, perturbations on the target molecules can be reduced. Because of this long measurable distance, together with a wider applicability to different sample states, pulsed ESR techniques complement conventional techniques of structural biology such as solution/solid state NMR and X-ray crystallography.

In-cell NMR spectroscopy, an MR-based in situ observation of proteins within living cells, has been successfully employed for the study of the conformations and interactions of proteins in Escherichia coli cells[23,24] and oocytes of Xenopus laevis.[25,26] Recently, in-cell NMR experiments using mammalian somatic cells were reported.[27] On the other hand, to the best of our knowledge, measurement of interspin distances of SDSL proteins inside cells by pulsed ESR methods has not been previously reported. In Chapter 3, I report the feasibility of DEER experiments for distance measurements of SDSL proteins inside oocytes of the African clawed frog, Xenopus laevis.

1.4 Optical-detected magnetic resonance selective imaging of fluorescent nanodiamonds

Fluorescence microscopy is a powerful methodology to understand the molecular dynamics of complex biological processes in living organisms. Despite the advent of novel instrumentation such as super-resolution microscopy[28], fluorescent probes[29] remain the key determinant of the image quality as well as the resolution. Recent developments of imaging techniques[1] and fluorescent probes[29-21] have enabled fluorescence microscopy to observe localization and dynamics of biomolecules at higher resolution than the diffraction limit even at single-molecule level[33-36].

However, such sensitive detection is often hampered by autofluorescence from endogenous molecules, which may greatly confound the signal from target fluorescent probes. The standard procedure to avoid this problem is to label target biomolecules with fluorescent probes that emit color different from that of autofluorescence. Despite the wide color availability of fluorescent probes including organic dyes, quantum dots, and fluorescent proteins[2,6], autofluorescence often cannot be effectively removed by the procedure due to the fluorescence spectral overlap between the probes and autofluorescence. Here, we report on new fluorescence microscopy for real-time background-free imaging and orientation tracking of fluorescent nanodiamonds (FNDs) containing nitrogen-vacancy centers (NVCs) in vivo.

NVC is a crystal defect consisting of a nitrogen atom and the adjacent atomic carbon vacancy in diamond[37]. Owing to its remarkable physical properties, the defect attracts a growing attention in physical sciences such as quantum computing[38] and nano-scale magnetometry[39,40]. In life sciences, FND has been proposed as new labeling agents for fluorescence microscopy[41]. FNDs have been imaged inside living HeLa cells[42-44] and a model organism, Caenorhabditis elegans [45] by confocal microscopy. Besides the biocompatibility[45] and flexible labeling capability[46] of diamond nanoparticles, fluorescence properties of NVC are superior to those of widely-used fluorescent probes: NVC exhibits neither photobleaching nor blinking[43] unless the diameter of diamond is less than 5 nm[47]. Moreover, fluorescence spectrum of NVC (600−850 nm) is ideal for cell, tissue, and whole-body imaging because within the near-infrared window most tissues have minimal absorbance[48], less autofluoescence and light scattering than in the shorter wavelength part of the spectrum[49].

Another unique fluorescence property of NVC is that the fluorescence intensity can be modulated by microwave (MW) based on optically detected magnetic resonance[50] (ODMR). We can use optically pumped electron spin instead of thermal Boltzmann polarized electron spin in ODMR measurement of NVCs. The magnetically sensitive fluorescence emission is special and thus FND is expected to find novel applications in life sciences such as electromagnetic sensing of ion channel activity[51]. In fact, a recent study reported that orientation of FNDs in living HeLa cells could be tracked by continuous ODMR monitoring[44].

In Chapter 4, I report a new fluorescence microscopy using fluorescent nanodiamonds FNDs containing nitrogen-vacancy centers NVCs. Fluorescence modulation using ODMR allows us to perform real-time background-free selective imaging of multiple FNDs inside C. elegans and higher animal, nude mouse. Moreover, ODMR with an externally applied magnetic field enables us to determine two rotational angles of FNDs in C. elegans with ~1° accuracy. We detect different intestinal activity among living, dead, and IP3-receptor mutated C. elegans, which agrees well with a past observation[52]. Besides the fluorescence modulation capability, FNDs emit tissue-transparent, near-infrared fluorescence and exhibit neither photobleaching nor blinking. Thus, the fluorescence microscopy reported here will be widely applicable to in vivo imaging.

Reference

1 Weissleder, R.; Reimer, P.; Lee, A.S.; Wittenberg, J.; Brady, T.J. MR Receptor Imaging: Ultrasmall Iron Oxide Particles Targeted to Asialoglycoprotein *Receptors. Am. J. Roentgenol.* **1990**, 155, 1161–1167.

2 Louie, A.Y.; Huber, M. M.; Ahrens, E.T.; Rothbacher, U.; Moats, R.; Jacobs, R.E.; Fraser, S.E.; Meade, T.J. In Vivo Visualization of Gene Expression Using Magnetic Resonance Imaging. *Nat. Biotechnol.* **2000**, 18, 321–325.

3 Gambhir, S.S.; Barrio, J.R.; Phelps, M.E.; Iyer, M.; Namavari, M.; Satyamurthy, N.; Wu, L.; Green, L.A.; Bauer, E.; MacLaren, D.C.; Nguyen, K.; Berk, A.J.; Cherry, S.R.; Herschman, H.R. Imaging Adenoviral-directed Reporter Gene Expression in Living Animals with Positron Emission Tomography. *Proc. Natl. Acad. Sci. USA* **1999**, 96, 2333–2338.

4 Mayerhofer, R.; Araki, K.; Szalay, A.A. Monitoring of Spatial Expression of Firefly Luciferase in Transformed Zebrafish. *J. Biolumin. Chemilumin.* **1995**, 10, 271–275.

5 Rehemtulla, A.; Stegman, L.D.; Cardozo, S.J.; Gupta, S.; Hall, D.E.; Contag, C.H.; Ross, B.D. Rapid and Quantitative Assessment of Cancer Treatment Response Using In Vivo Bioluminescence Imaging. *Neoplasia* **2000**, 2, 491–495.

6 Halpern, J. Contrast-enhanced Ultrasound Imaging of Prostate Cancer. *Rev. Urol.* **2006**, 8, S29–S37.

7 G. J. KARABATSOCS. ,E . ORZECHJ,R . , AND S. MEYERSON, Carbonium Ion Rearrangements. VI. Mechanism of the Reaarangement of Neopentyl Compounds. *J. Am. Chem. Soc.* **1964**, 86, 1994.

8 A. A. Maudsley and R. R. Ernst, Indirect detection of magnetic resonance by heteronuclear two-dimensional spectroscopy. *Chem. Phys. Lett.* **1977**, 50, 368.

9 Examples of signal-switching NMR/MRI probes, see refs. 314: J. L. Major, G. Parigi, C. Luchinat, T. J. Meade, *Proc. Natl. Acad. Sci. U.S.A.* **2007**, 104, 13881.

10 A. Y. Louie, M. M. Hüber, E. T. Ahrens, U. Rothbächer, R. Moats, R. E. Jacobs, S. E. Fraser, T. J. Meade, *Nat. Biotechnol.* **2000**, 18, 321.

11 R. A. Moats, S. E. Fraser, T. J. Meade, *Angew. Chem., Int. Ed. Engl.* **1997**, 36, 726.

12 L.Liu, V. D. Kodibagkar, J.-X. Yu, R. P. Mason, *FASEB J.* **2007**, 21, 2014.

13 J.-X. Yu, V. D. Kodibagkar, W. Cui, R. P. Mason, *Curr. Med. Chem.* **2005**, 12, 819.

14 S.Mizukami, R. Takikawa, F. Sugihara, Y. Hori, H. Tochio, M. Wälchli, M. Shirakawa, K. Kikuchi, *J. Am. Chem. Soc.* **2008**, 130, 794.

15 J. M. Perez, L. Josephson, T. O'Loughlin, D. Högemann, R. Weissleder, *Nat. Biotechnol.* **2002**, 20, 816.

16 E. Garanger, S. A. Hilderbrand, J. T. Blois, D. E. Sosnovik, R. Weissleder, L.

Josephson, *Chem. Commun.* **2009**, 4444.

17 M. Woods, D. E. Woessner, A. D. Sherry, *Chem. Soc. Rev.* **2006**, 35, 500.

18 K. Hanaoka, K. Kikuchi, Y. Urano, M. Narazaki, T. Yokawa, S. Sakamoto, K. Yamaguchi, T. Nagano, *Chem. Biol.* **2002**, 9, 1027.

19 K. Tanaka, K. Inafuku, Y. Chujo, Bioorg. *Med. Chem.* **2008**, 16, 10029.

20 Y. Takaoka, T. Sakamoto, S. Tsukiji, M. Narazaki, T. Matsuda, H. Tochio, M. Shirakawa, I. Hamachi, *Nat. Chem.* **2009**, 1, 557.

21 Borbat, P. P.; McHaourab, H. S.; Freed, J. H. *J. Am. Chem. Soc.* **2002**, 124, 5304–14.

22 Altenbach, C.; Kusnetzow, A. K.; Ernst, O. P.; Hofmann, K. P.; Hubbell, W. L. *Proc. Natl. Acad. Sci. U.S.A.* **2008**, 105, 7439–44.

23 Serber, Z.; Corsini, L.; Durst, F.; Dotsch, V. *Methods Enzymol.* **2005**, 394, 17–41.

24 Li, C.; Charlton, L. M.; Lakkavaram, A.; Seagle, C.; Wang, G.; Young, G. B.; Macdonald, J. M.; Pielak, G. J. J. Am. Chem. Soc. 2008, 130, 6310–1. (c) Burz, D. S.; Dutta, K.; Cowburn, D.; Shekhtman, A. *Nat Methods* **2006**, 3, 91–3.

25 Sakai, T.; Tochio, H.; Tenno, T.; Ito, Y.; Kokubo, T.; Hiroaki, H.; Shirakawa, M. *J. Biomol. NMR* **2006**, 36, 179–88.

26 Selenko, P.; Frueh, D. P.; Elsaesser, S. J.; Haas, W.; Gygi, S. P.; Wagner, G. Nat.

Struct. *Mol. Biol.* **2008**, 15, 321–9.

27 Inomata, K.; Ohno, A.; Tochio, H.; Isogai, S.; Tenno, T.; Nakase, I.; Takeuchi, T.; Futaki, S.; Ito, Y.; Hiroaki, H.; Shirakawa, M. *Nature* **2009**, 458, 106–9.

28 Huang, B., Babcock, H. & Zhuang, X. Breaking the diffraction barrier: super-resolution imaging of cells. *Cell* **2010**, 143, 1047-1058

29 Giepmans, B. N., Adams, S. R., Ellisman, M. H. & Tsien, R. Y. The fluorescent toolbox for assessing protein location and function. *Science* **2006**, 312, 217-224.

30 Shaner, N. C., Steinbach, P. A. & Tsien, R. Y. A guide to choosing fluorescent proteins. *Nat. Methods* **2005**, 2, 905-909.

31 Marriott, G. et al. Optical lock-in detection imaging microscopy for contrast-enhanced imaging in living cells. *Proc. Natl. Acad. Sci. USA* **2008**, 105, 17789-17794.

32 Grotjohann, T. et al. Diffraction-unlimited all-optical imaging and writing with a photochromic GFP. *Nature* **2011**, 478, 204-208.

33 Toprak, E. & Selvin, P. R. New fluorescent tools for watching nanometer-scale conformational changes of single molecules. *Annu. Rev. Biophys. Biomol. Struct.* **2007**, 36, 349-369.

34 Joo, C., Balci, H., Ishitsuka, Y., Buranachai, C. & Ha, T. Advances in single-molecule fluorescence methods for molecular biology. *Annu. Rev. Biochem.* **2008**, 77, 51-76.

35 Beausang, J. F., Schroeder 3rd, H. W., Nelson, P. C. & Goldman, Y. E. Twirling of actin by myosins II and V observed via polarized TIRF in a modified gliding assay. *Biophys. J.* **2008**, 95, 5820–5831.

36 Lord, S. J., Lee, H. L. & Moerner, W. E. Single-molecule spectroscopy and imaging of biomolecules in living cells. Anal. Chem. 2010, 82, 2192-2203.

37 Aharonovich, I., Greentree, A. D. & Prawer, S. Diamond photonics. *Nature Photon.* **2011**, 5, 397-405.

38 Dutt, M. V. G. et al. Quantum register based on individual electronic and nuclear spin qubits in diamond. *Science* **2007**, 316, 1312-1316.

39 Balasubramanian, G. et al. Nanoscale imaging magnetometry with diamond spins under ambient conditions. *Nature* **2008**, 455, 648-651.

40 Grinolds, M. S. et al. Quantum control of proximal spins using nanoscale magnetic resonance imaging. *Nature Phys.* **2011**, 7, 687-692

41 Ho, D. Beyond the sparkle: the impact of nanodiamonds as biolabeling and therapeutic agents. *ACS Nano* **2009**, 3, 3825-3829.

42 Chang, H. C. et al. Mass production and dynamic imaging of fluorescent nanodiamonds. *Nature Nanotech.* **2008**, 3, 284-288.

43 Faklaris, O. et al. Comparison of the photoluminescence properties of semiconductor

quantum dots and non-blinking diamond nanoparticles. Observation of the diffusion of diamond nanoparticles in living cells. *J. Eur. Opt. Soc. Rapid. Publ.* **2009**, 4, 09035.

44 McGuinness, L. P. et al. Quantum measurement and orientation tracking of fluorescent nanodiamonds inside living cells. *Nature Nanotech.* **2011**, 6, 358-363.

45 Mohan, N., Chen, C.-S., Hsieh, H.-H., Wu, Y.-C. & Chang, H.-C. In vivo imaging and toxicity assessments of fluorescent nanodiamonds in Caenorhabditis elegans. *Nano Lett.* **2010**, 10, 3692–3699.

46 Chang, I. P. et al. Facile surface functionalization of nanodiamonds. *Langmuir* **2010**, 26, 3685-3689.

47 Bradac, C. et al. Observation and control of blinking nitrogen-vacancy centres in discrete nanodiamonds. *Nature Nanotech.* **2010**, 5, 345-349.

48 Jobsis, F. F. Noninvasive, infrared monitoring of cerebral and myocardial oxygen sufficiency and circulatory parameters. *Science* **1977**, 198, 1264-1267.

49 Ntziachristos, V. Going deeper than microscopy: the optical imaging frontier in biology. *Nat. Methods* **2010**, 7, 603-614.

50 Gruber, A. et al. Scanning confocal optical microscopy and magnetic resonance on single defect centers. *Science* **1997**, 276, 2012-2014.

51 Hall, L. T. et al. Monitoring ion-channel function in real time through quantum

decoherence. Proc. Natl. Acad. Sci. USA 2010, 107, 18777-18782.

52 Dal Santo, P., Logan, M. A., Chisholm, A. D. & Jorgensen, E. M. The inositol trisphosphate receptor regulates a 50-second behavioral rhythm in C. elegans. *Cell* **1999**, 98, 757-767.

Chapter 2

Turn-on detection of targeted biochemical reactions by triple resonance NMR analysis using isotope-labeled probe

2.1 Introduction

There has been a long-term effort into the analysis of specific chemical events in complex biological systems, and metabolic profiling is one of the most intriguing targets among a variety of events. Metabolites are chemical products resulting from essential biological activities and, therefore, can be good biomarkers to reveal the physiological or chemical status of cells, tissues, and organs.

NMR/MRI-based technology is one of the most promising techniques for the analysis of such biochemical (metabolic) reactions. However, the detection of target metabolites or biochemical reactions of interest is often difficult because of spectral overlaps with a large number of biological components.

To overcome this, attempts to trace metabolic pathways by the administration of stable isotope-labeled compounds as probes has been reported.[1] In principle, these isotope-labeled compounds are highly potential probes since these are NMR-sensitive and constitutively NMR-active. However, this advantage can also be a disadvantage since, for the same reason, these probes and derived various intermediates/metabolites all serve as possible origins of background noise signals, and thus target metabolite should be carefully discriminated from others by the precise analysis of the chemical shifts, typically by measuring the 2D NMR spectra.[1,2] Especially, such spectral overlaps are problem for detection of ^{1}H, the most sensitive and thus attractive nucleus, due to its small chemical shift range.

In this context, ideal chemical probes are those with a signal on/off device, that are otherwise NMR-silent and is rendered NMR-active only when accumulated at target sites and subjected to specific biochemical events.[3-14] In this work, we have used a triple resonance NMR technique for the detection of isotopically labeled metabolites generated in cells and in injected mice with high selectivity. In addition, for the first time, we report on a signal-activatable glucose-based probe, which turns "on" its ^{1}H NMR signals as a result of target anaerobic glycolytic reaction.

2.2 Selectivity of triple resonance NMR

The triple resonance technique is a method to correlate three NMR-active nuclei with different Lamor frequencies. For example, when the pulse scheme allows the magnetic coherence of 1H to transfer to two successive ^{13}C nuclei with different Lamor frequencies through scalar couplings, only the proton in the particular sequence ^{1}H-^{13}C-^{13}C is detectable. Due to the low natural abundance of ^{13}C (1.1%), the probability of a naturally occurring ^{1}H-^{13}C-^{13}C sequence is as low as 0.0001%, suggesting that the triple resonance technique can markedly improve the selectivity of detection of a target molecule having ^{1}H-^{13}C-^{13}C by lowering the background signal.[15]

2.3 Turn-on detection of anaerobic glycolysis

As a model metabolic reaction for demonstrating the proof-of-concept of our idea, we chose the glucose-to-lactate production. Among the stable isotopomers for metabolic analysis by NMR, ^{13}C-labeled glucose is one of the most intensively studied. Glucose is a common source of energy in cells and is converted to a variety of metabolites during glycolysis. Among these, lactate H_3C-CH(OH)-CO_2H is a key end metabolite. In particular, in tumor cells, glucose is actively converted to lactate through an anaerobic glycolytic pathway.[16,17] We challenged to develop a method to detect generation of lactate from glucose using isotope-enriched glucose as a probe that turns from "off" to "on" its own ^1H NMR signals in synchronization with a target anaerobic glycolytic reaction (Figure 2-1).

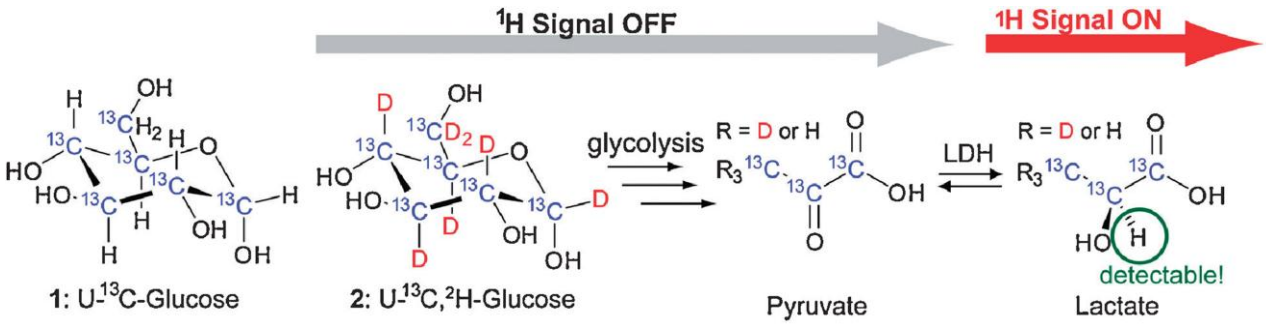

Figure 2-1 Chemical structure of the glucose-based probes 1 and 2, and a schematic drawing showing how the glucose probe 2 works as an OFF-to-ON-type NMR probe for the production of a lactate biomarker.

2.4 Triple resonance NMR measurement of chemically synthesized ^{13}C-labeled lactate

First, we measured a triple resonance NMR spectrum of chemically synthesized ^{13}C-labeled lactate. We used a pulse sequence for the detection of a ^{1}H bound to an aliphatic ^{13}C, which in turn was connected to a carbonyl ^{13}C (^{1}H-{^{13}C-^{13}CO}).[18] The conventional ^{1}H NMR spectrum of 1,2,3-^{13}C-labeled racemic lactate, prepared by chemical reduction of 1,2,3-^{13}C-labeled pyruvate using $NaBH_4$,[19] in D_2O shows two double multiplets attributable to methine protons (2-C, 4.21 ppm, JCH = 147 Hz) and methyl protons (3-C, 1.30 ppm, JCH = 129 Hz) (Figure 2-2a[21]). In marked contrast, only methine protons (2-C) were detected in the triple resonance experiment (Figure 2-2b[21]) with a detection limit of 77 μM under our experimental conditions

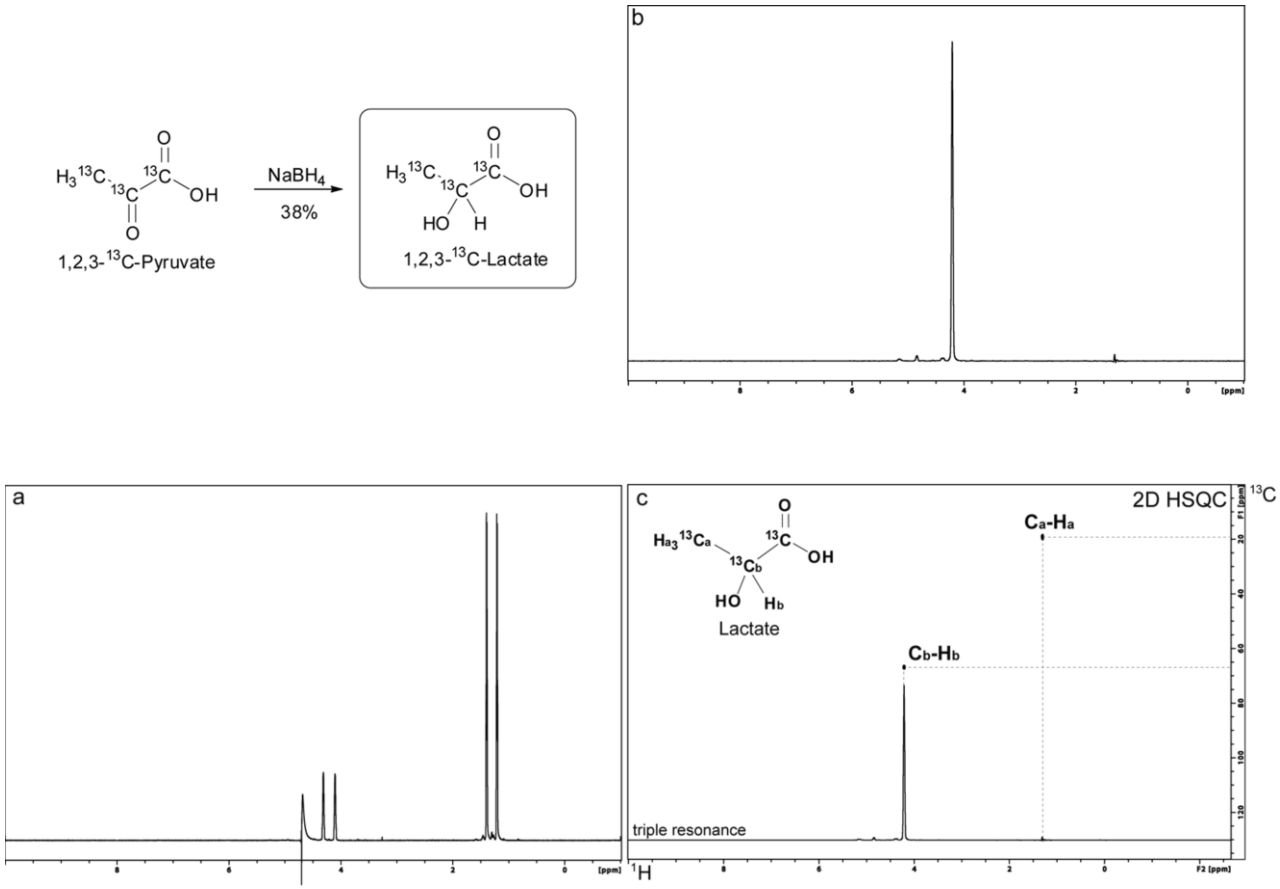

Figure 2-2 NMR spectra of chemically synthesized $^{13}C_3$-lactate. a) Single 1H, b) triple resonance $^{1}H–\{^{13}C–^{13}CO\}$ and c) 2D $^{1}H–^{13}C$ HSQC spectra of chemically synthesized lactate (1 mM) in D_2O. The 2D HSQC spectrum c) is merged with the 1D $^{1}H–\{^{13}C–^{13}CO\}$ triple resonance spectrum b).

2.5 Probe optimization to suppress the signals from various glycolytic metabolites other than lactate

Once the triple resonance technique was optimized to detect targeted lactate, we moved on to sensing of the biomarker lactate using isotope-labeled glucose as a precursor probe. Initially, we used the glucose probe 1 (Figure 2-1), where all the carbon atoms were enriched with ^{13}C. Again, our purpose was to develop an OFF-to-ON-type metabolic sensing probe that would ideally be undetected until subjected to the metabolic reaction of concern. The ^{13}C-labeled glucose probe 1 is not ideal in this respect, since probe 1 and its glycolysis intermediates have many ^{1}H-^{13}C-^{13}C sequences, while not of the ^{1}H-^{13}C-^{13}CO-type, which could possibly give rise to undesired ^{1}H signals, even through the triple resonance selection scheme. This was indeed the case. The glucose probe 1 afforded undesired signals even without the metabolic reactions (Figure 2-3[21]).

Thus, we redesigned the probe and used the fully ^{13}C- and ^{2}H-labeled glucose 2. Since the number of ^{13}C-bound ^{1}H in probe 2 and its metabolites up to pyruvate in the first nine enzymatic reactions are highly suppressed (Figure 2-4[21]), they should be undetectable under the triple resonance conditions. In the final step of glycolysis, an NMR-active (detectable) species is generated, where the pyruvate is converted (reduced) to lactate by lactate dehydrogenase (LDH) with concomitant incorporation of ^{1}H from the coenzyme NADH to give a detectable ^{1}H-{^{13}C-^{13}CO} sequence. Therefore, glucose probe 2 can be a turn-on sensing probe to selectively monitor an anaerobic production of lactate (Figure 2-1).

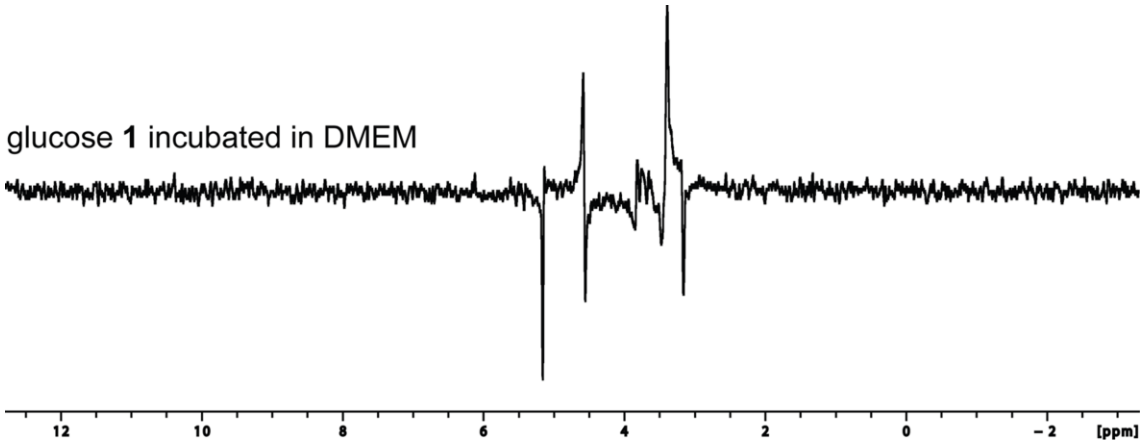

Figure 2-3 Triple resonance $^{1}H–\{^{13}C–^{13}CO\}$ NMR spectrum of DMEM medium containing ^{13}C-labeled glucose probe 1 (6.5 mM) incubated for a period of 24 h.

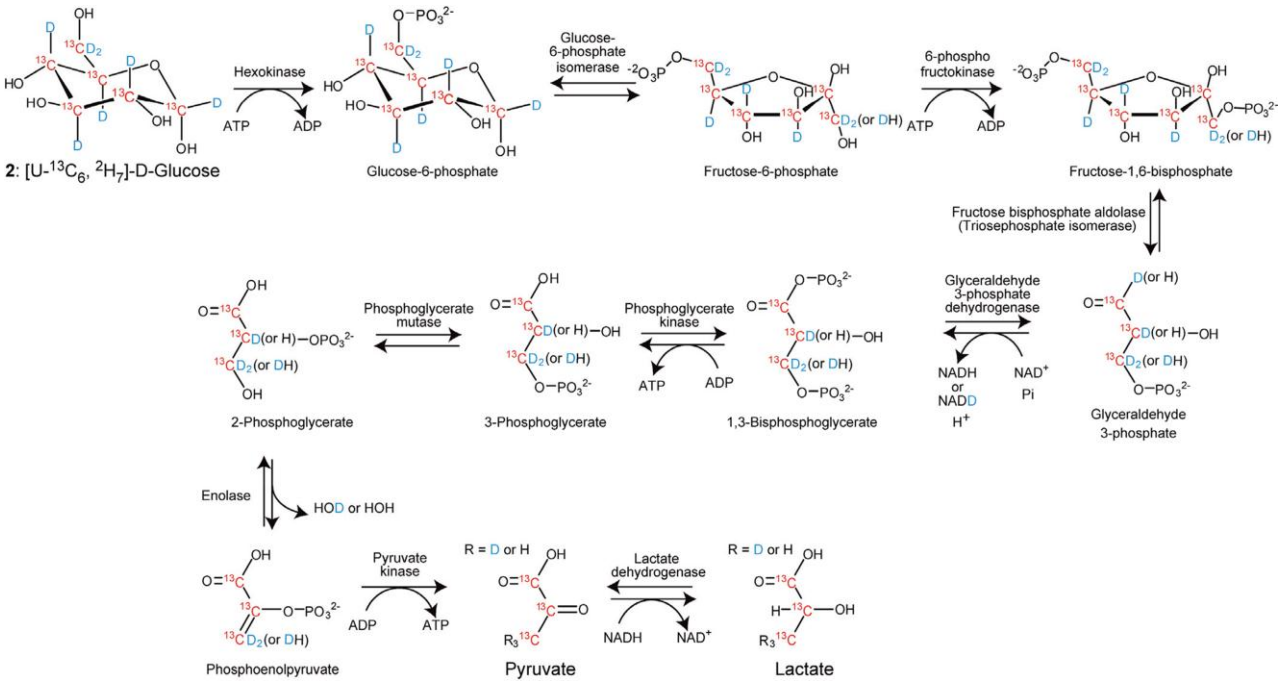

Figure 2-4 Proposed reaction pathway showing how the glucose probe 2 is converted to lactate by an anaerobic glycolytic reaction. The 13C and 2H(D) nuclei are shown in red and blue, respectively.

2.6 Monitoring the glucose-to-lactate conversion in cultured cells

We were first challenged to monitor the glucose-to-lactate conversion in cultured HeLa cells. The fully $^{13}C/^{2}H$-labeled glucose probe 2 (6.5 mM) was added to HeLa cells (2.4×10^6 cells) in a DMEM medium. After incubation at 37 °C for 24 h, the medium was collected, lyophilized, resuspended in D_2O, and subjected to NMR analysis. As shown in Figure 2-5, a single signal (4.02 ppm) was observed in the triple resonance ^{1}H-{^{13}C-^{13}CO} NMR analysis, which was assigned and confirmed by 2D ^{1}H-^{13}C HSQC analysis (Figure 2-6 vs. 2-2c[21]) to the methane protons of the lactate metabolically produced in the HeLa cells. Importantly, completely no signal was detected from glucose probe 2 incubated in the absence of HeLa cells (Figure 2-5). These results clearly indicate that the fully $^{13}C/^{2}H$-labeled glucose 2 works as an OFF-to-ON switching NMR probe to detect lactate production from glucose in cells selectively.

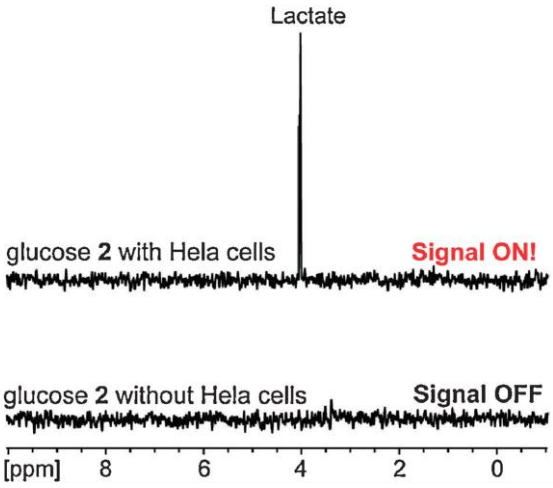

Figure 2-5 NMR spectroscopic observations on the conversion of glucose to lactate in cells. Triple resonance 1H NMR spectra (1H-{13C-13CO}) of the DMEM containing glucose probe 2 incubated with (upper) or without (lower) HeLa cells for a period of 24 h.

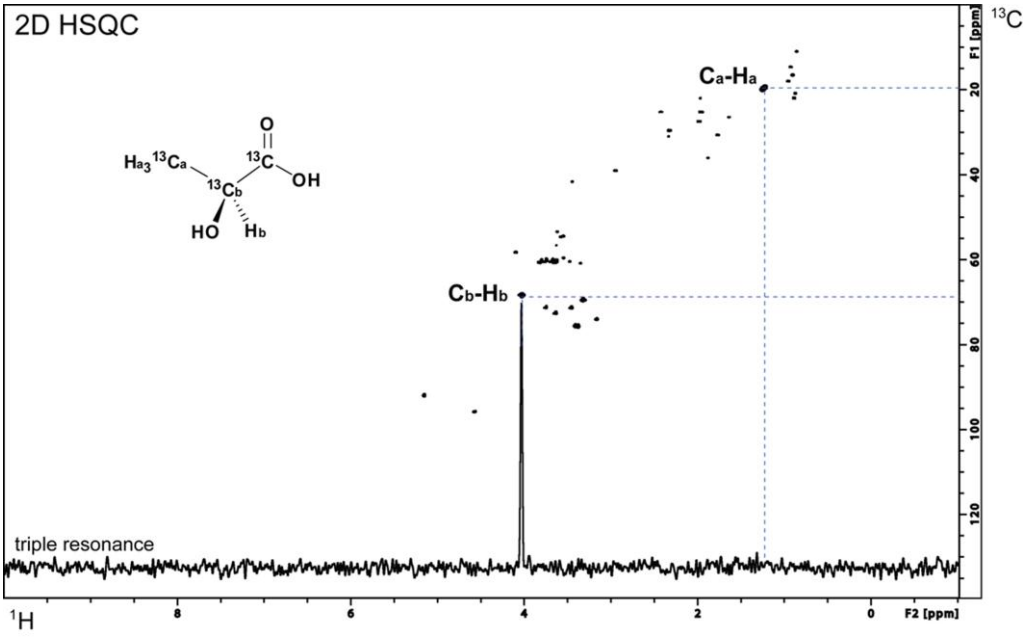

Figure 2-6 2D ^{1}H–^{13}C HSQC spectrum of metabolites from glucose probe 2 (6.5 mM) incubated in DMEM with HeLa cells. The 2D HSQC spectrum is merged with the 1D ^{1}H–{^{13}C–^{13}CO} triple resonance spectrum (Figure 2-5, upper).

2.7 Turn-on lactate-sensing to metabolic reaction analysis in mice

Then, we applied our turn-on lactate-sensing approach to metabolic reaction analysis in mice. Glucose probe 2 (3 g/kg body weight) was infused via the tail vein into a mouse bearing subcutaneously inoculated murine colon adenocarcinoma C-26. After a period of 1 h, the tumor was collected, lysed, redissolved in D_2O, and subjected to NMR analysis. Figure 2-7 shows the ^{1}H NMR spectra of the tumor in single (^{1}H, upper spectrum), double (^{1}H-{^{13}C}, middle spectrum), and triple resonance (^{1}H-{^{13}C-^{13}CO}, lower spectrum) experiments. As can be clearly seen in Figure 2-7, the conventional ^{1}H (upper) spectrum is useless due to the presence of a variety of signals. The double resonance spectrum (^{13}C-selected 1H, middle spectrum) still displays more than 10 signals. In marked contrast, only two signals, a major signal at 4.26 ppm and a minor signal at 4.02 ppm, were observed in the triple resonance spectrum (lower spectrum), which were assigned using 2D ^{1}H-^{13}C HSQC analysis to the methine protons of lactate (^{1}H-^{13}C(OH)-^{13}C=O) and alanine (^{1}H-^{13}C(NH_2)-^{13}C=O), respectively, the latter compoundbeing produced from pyruvate by a transaminase reaction (Figure 2-8).[20,21] Thus, the present signal turn-on strategy using a combination of the triple resonance technique and a dual $^{13}C/^{2}H$-labeled probe is applicable to ex vivo analysis.

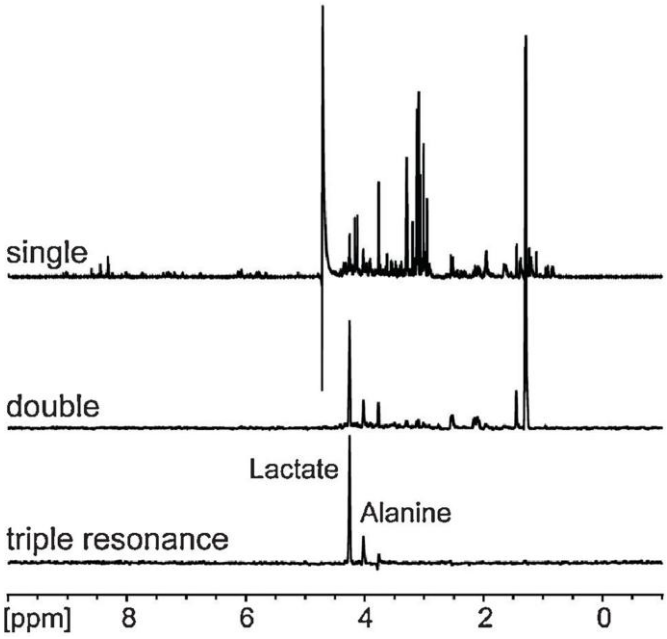

Figure 2-7 NMR spectroscopic observations on the conversion of glucose to lactate in mice. Single (1H), double (1H-{13C}), and triple (1H-{13C-13CO}) resonance NMR spectra of the extracts from a tumor (murine colon adenocarcinoma C-26) in a mouse, which was infused with glucose probe 2 via the tail vein. Detection of lactate in tumor by triple resonance NMR was successfully repeated in at least five separate experiments.

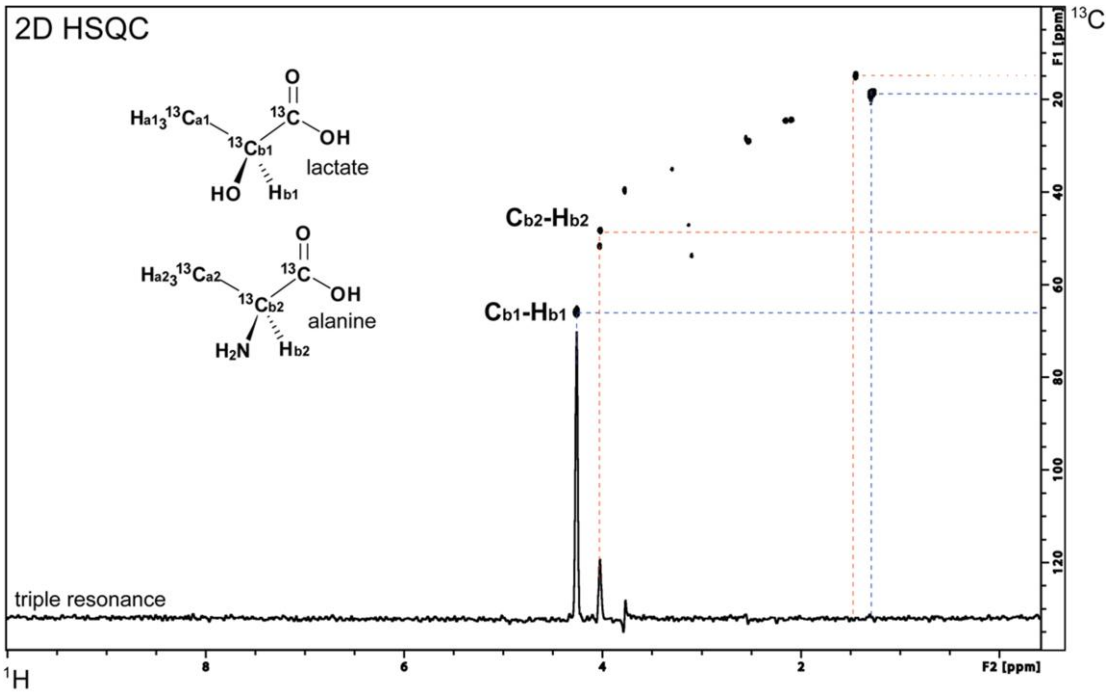

Figure 2-8 2D ^{1}H–^{13}C HSQC spectrum of metabolites of a lysed tumor (murine colon adenocarcinoma C26) from a mouse, infused with glucose probe 2 via the tail vein. The 2D HSQC spectrum is merged with the 1D ^{1}H–{^{13}C–^{13}CO} triple resonance spectrum (Figure 2-7, lower). NMR peaks assigned as alanine were confirmed by measuring 2D ^{1}H–^{13}C HSQC spectrum of the lysed tumor in the presence of commercial alanine as an authentic sample.

2.8 Conclusion

In conclusion, this work reveals the potential utility of triple resonance NMR technique for monitoring of particular biochemical events in situ. Suppression of the background noise is not perfect in double resonance ^{1}H-{^{13}C} experiments but becomes satisfactory using a triple resonance technique for selective detection of lactate-producing reaction. Importantly, the present 1H probe is a novel “switch-on” type, which is otherwise NMR-silent and is rendered active only when transformed into the target metabolite by the metabolic reaction in concern. The method thus allows simple and unambiguous detection of specific metabolic event without requiring laborious and possibly misleading chemical shift analysis of the probe and its (various) metabolites. The present strategy is also applicable to other NMR-active (I = 1/2) nuclei, such as ^{15}N. Since sequences such as H-C-C and H-C-N are common in biorelevant molecules, there are plenty of potential candidate molecules as biomarkers that can be detected using the present technique. Conceptually, this approach can be applied for in vivo MRI/MRS and further challenge is now underway along these lines.

2.9 Methods

2.9.1 Synthesis

General. The reagents and solvents used were purchased from standard suppliers and used without further purification. The NMR spectra were measured using a Bruker Avance 700 spectrometer. The EI mass spectrum was recorded using a JEOL JMS SX102A spectrometer.

Synthesis of 1,2,3-^{13}C-labeled racemic lactate. $NaBH_4$ (18 mg, 0.49 mmol) was added to a reaction solution of [1,2,3-$^{13}C_3$]-sodium pyruvate (99 % ^{13}C; Isotec Inc.) (51 mg, 0.45 mmol) in H_2O (5 mL) on ice. The mixture was stirred for a period of 4 h at room temperature, and quenched by the addition of a ^{1}N HCl solution. The solvent was removed in vacuo, and the resulting residue was purified using gel permeation chromatography as a colorless oil (yield = 38%): ^{1}H NMR (D_2O, 700 MHz), Figure 2-2a; ^{13}C NMR (D_2O, 176 MHz) δ = 179.3 (m, C1), 66.7 (m, C2), 19.3 (m, C3); HRMS (EI): *m/z* calc. for $^{13}C_3H_6O_3$ [M^+] = 93.0418, found = 93.0416.

2.9.2 NMR analyses

General. All the NMR spectra were acquired at 298 K on a Bruker Avance 700

spectrometer equipped with a 5 mm TCI CryoProbe. All one-dimensional triple resonance spectra were obtained by using a 3D HCACO pulse sequence,[19] which is commonly used to assign the backbone chemical shifts of proteins, with slight modification for the one-dimensional proton experiments. The size of the FID was 2048 complex points, and the spectral width was 11261.26 Hz with an acquisition time of 90.98 ms. The obtained FID was apodized with a squared cosine-bell window function, and zero filled to 8192 points prior to the Fourier transformation. All 2D ^{1}H-^{13}C HSQC spectra were acquired at a 1H frequency of 700.18 MHz with a ^{1}H spectral width of 9328.36 Hz and a ^{13}C spectral width of 35213.49 Hz. The matrix size was 1024*×128* with acquisition times of 3.64 (t_1) and 109.82 ms (t_2). Data processing and analysis were performed using the Topspin 2.1 (Bruker Biospin, Karlsruhe, Germany).

Metabolic reaction in HeLa cells: glucose to lactate. HeLa cells (2.4×10^6 cells) were incubated in DMEM (+FBS, AB) containing 6.5 mM [U-$^{13}C_6$, 1,2,3,4,5,6,6-$^{2}H_7$]-D-glucose (99% ^{13}C, 97-98% ^{2}H; Cambridge Isotope Laboratories Inc.) at 37 °C under 5% CO_2 (starting density = 2.4×10^5 cells/mL). After a period of 24 h, the medium was collected and lyophilized, redissolved in D_2O (1 mL), and centrifuged at 4,500 rpm for a period of 5 min. An aliquot of the supernatant (50 μL) was diluted with D2O (450 μL) and subjected to NMR analysis (conditions for triple resonance analysis = 256 scans with a measurement time of approximately 5 min).

Glucose-to-lactate metabolic reaction in a mouse. Female BALB/cCrSlc mice (Shimizu Laboratory Supplies Co. Ltd., Kyoto, Japan) weighing approx. 15 g were used in the experiments. These were inoculated subcutaneously with 4.0×10^6 cells of colon 26 in the left hind limb 9 d before the experiments. A tumor-bearing mouse that fasted for a period of 24 h (with free access to water) was injected intravenously with a bolus of [U-$^{13}C_6$, 1,2,3,4,5,6,6-$^{2}H_7$]-D-glucose (3.0 g/kg body weight) via the tail vein. The mouse was killed under anesthesia using diethylether one hour after the administration of the labeled glucose. The entire tumor was harvested and homogenized in 10% trichloroacetic acid (TCA) using a Qiagen TissueLyser. After incubation for a period of 30 min on ice, the homogenates were centrifuged at 12,000 rpm for a period of 5 min at 4 °C and the aqueous extracts were taken up. The residues were washed with 10% TCA and the supernatant was collected after centrifugation. The combined aqueous extracts were lyophilized to dryness and dissolved in D_2O (700 μL). After centrifugation at 13,200 rpm for a period of 30 min, the supernatant was taken for NMR analysis (conditions for triple resonance analysis = 1024 scans with a measurement time of approximately 20 min).

References

1 T. W.-M. Fan, A. N. Lane, *Prog. Nucl. Magn. Reson. Spectrosc.* **2008**, 52, 69, and references therein.

2 A. N. Lane, T. W.-M. Fan, R. M. Higashi, *IUBMB Life* **2008**, 60, 124.

3 Examples of signal-switching NMR/MRI probes, see refs. 314: J. L. Major, G. Parigi, C. Luchinat, T. J. Meade, *Proc. Natl. Acad. Sci. U.S.A.* **2007**, 104, 13881.

4 A. Y. Louie, M. M. Hüber, E. T. Ahrens, U. Rothbächer, R. Moats, R. E. Jacobs, S. E. Fraser, T. J. Meade, *Nat. Biotechnol.* **2000**, 18, 321.

5 R. A. Moats, S. E. Fraser, T. J. Meade, *Angew. Chem., Int. Ed. Engl.* **1997**, 36, 726.

6 L.Liu, V. D. Kodibagkar, J.-X. Yu, R. P. Mason, *FASEB J.* **2007**, 21, 2014.

7 J.-X. Yu, V. D. Kodibagkar, W. Cui, R. P. Mason, *Curr. Med. Chem.* **2005**, 12, 819.

8 S.Mizukami, R. Takikawa, F. Sugihara, Y. Hori, H. Tochio, M. Wälchli, M. Shirakawa, K. Kikuchi, *J. Am. Chem. Soc.* **2008**, 130, 794.

9 J. M. Perez, L. Josephson, T. O'Loughlin, D. Högemann, R. Weissleder, *Nat. Biotechnol.* **2002**, 20, 816.

10 E. Garanger, S. A. Hilderbrand, J. T. Blois, D. E. Sosnovik, R. Weissleder, L. Josephson, *Chem. Commun.* **2009**, 4444.

11 M. Woods, D. E. Woessner, A. D. Sherry, *Chem. Soc. Rev.* **2006**, 35, 500.

12 K. Hanaoka, K. Kikuchi, Y. Urano, M. Narazaki, T. Yokawa, S. Sakamoto, K. Yamaguchi, T. Nagano, *Chem. Biol.* **2002**, 9, 1027.

13 K. Tanaka, K. Inafuku, Y. Chujo, *Bioorg. Med. Chem.* **2008**, 16, 10029.

14 Y. Takaoka, T. Sakamoto, S. Tsukiji, M. Narazaki, T. Matsuda, H. Tochio, M. Shirakawa, I. Hamachi, *Nat. Chem.* **2009**, 1, 557.

15 The triple resonance technique has been used mostly for the structural analysis of biological materials such as proteins. Application to metabolic analysis has also been challenged in a few examples only in plant, wherein discrimination of the target metabolites from other triple-resonance NMRactive ones including starting materials were based on precise chemical shift analysis, and not in a “turn-on” manner as demonstrated here. We utilized the triple resonance technique for the “turn-on” detection of the target metabolite. Examples, see: a) J. K. Gard, P. C. C. Feng, W. C. Hutton, *Xenobiotica* **1997**, 27, 633. b) W. C. Hutton, J. J. Likos, J. K. Gard, J. R. Garbow, J. Labelled *Compd. Radiopharm.* **1998**, 41, 87. c) J. K. Gard, W. C. Hutton, J. A. Baker, R. K. Singh, P. C. C. Feng, *Pestic. Sci.* **1999**, 55, 215.

16 O. Warburg, *Science* **1956**, 123, 309.

17 S. Walenta, W. F. Mueller-Klieser, *Semin. Radiat. Oncol.* **2004**, 14, 267.

18 L. E. Kay, M. Ikura, R. Tschudin, A. Bax, *J. Magn. Reson.* **1990**, 89, 496.

19 E. B. Reid, J. R. Siegel, *J. Chem. Soc.* **1954**, 520.

20 Recent report on pyruvate-to-alanine conversion, see: E. A. Mazzio, B. Smith, K. F. A. Soliman, *Cell Biol. Toxicol.* **2010**, 26, 177.

21 Supporting Information is available electronically on the CSJ-Journal Web site, http://www.csj.jp/journals/chem-lett/index.html.

Chapter 3

Distance Determination in Proteins inside Xenopus laevis Oocytes by Double Electron-Electron Resonance Experiments

3.1 Introduction

Pulsed ESR techniques, such as DEER (double electron–electron resonance) and electron DQC (double quantum coherence), combined with site-directed spin labeling (SDSL), are receiving increasing attention in structural biology because they provide a means for accurate determination of relatively long distances between electron spin centers introduced into proteins of interest.[1,2] With these methods, distributions of interspin distances of SDSL proteins in a range from 1.5 to 8 nm have been reported. This broad range of measurable distances is comparable to that of the FRET (Förster Resonance Energy Transfer) technique, but because the spin-label probes are smaller than the fluorophores, perturbations on the target molecules can be reduced. Because of this long measurable distance, together with a wider applicability to different sample states (e.g., crystallization is not required), pulsed ESR techniques complement conventional techniques of structural biology such as solution/solid state NMR and X-ray crystallography.

In-cell NMR spectroscopy, an MR-based in situ observation of proteins within living cells, has been successfully employed for the study of the conformations and interactions of proteins in Escherichia coli cells[3,4] and oocytes of Xenopus laevis.[5,6] Recently, we reported in-cell NMR experiments using mammalian somatic cells.[7] On the other hand, to the best of our knowledge, measurement of interspin distances of SDSL proteins inside cells by pulsed ESR methods has not been previously reported. In this study, we examined the feasibility of DEER experiments for distance measurements of SDSL proteins inside oocytes of the African clawed frog, Xenopus laevis.

3.2 Reductive conversion of the nitroxide radicals in oocytes

One intrinsic difficulty of ESR measurement of SDSL proteins inside cells comes from the short persistence of radical spins in cells. A nitroxide radical, the most commonly used radical species for SDSL, can be chemically reduced in the cytoplasmic environment. It was reported that the ESR signals of nitroxide radicals attached to the extracellular regions of membrane proteins disappeared after the protein had been internalized from the plasma membrane into the cytosol.[8] Therefore, the persistence of such radical species in cells is a major concern in performing the DEER experiments. Thus, we first examined the lifetime of nitroxide spin labels in Xenopus oocytes using continuous wave (CW)-ESR. A human ubiquitin derivative bearing cysteine substitutions at Ser20 and Gly35 (designated S20C-G35C) was labeled using 3-maleimido-PROXYL, which attaches nitroxide spin labels to the thiol groups of those cysteines[9] (Figure 3-1 and 3-2). It is important to note that the maleimide conjugation, unlike disulfide linkage, is resistant to reductive cleavage. The SDSL protein was injected into oocytes, which were then incubated for various periods and washed, and then frozen for CW-ESR measurement.

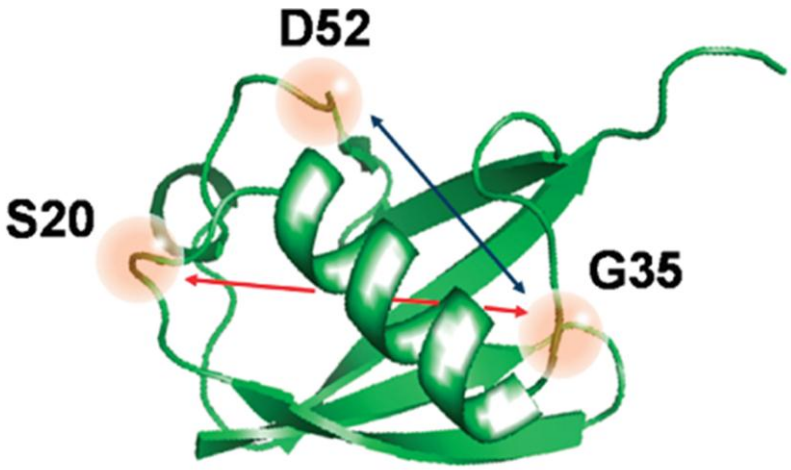

Figure 3-1 Ribbon diagram of the structure of ubiquitin. Two of the Three spin-labeled sites, Ser20, Gly35, and Asp52, were substituted with cysteine. Distances measured are indicated with red (S20-G35) and blue (G35-D52) arrows.

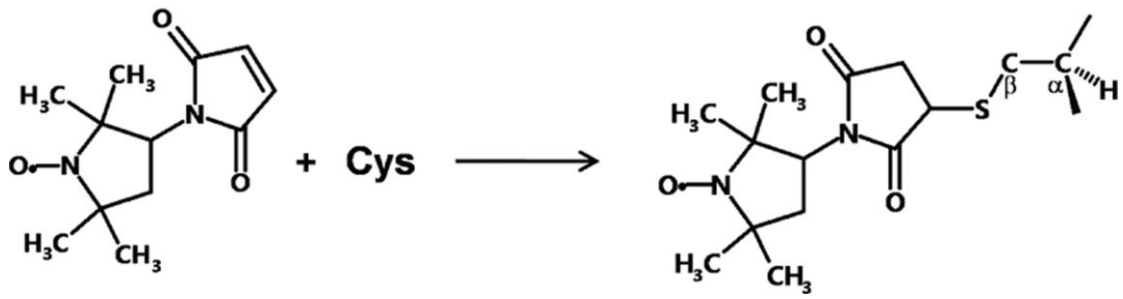

Figure 3-2 Site-directed spin labeling. two cysteines of Figure 3-1 (S20 and G35 or G35 and D52) were reacted with 3-maleimido-PROXYL.

The spectra of the oocytes displayed a pattern similar to that of an in vitro reference spectrum (Figure 3-3), suggesting the observed signals can be attributed to the nitroxide radicals. The ESR signal intensities decreased with increasing incubation time, presumably due to reductive conversion of the nitroxide radicals to ESR-silent hydroxyl amines. Each CW-ESR spectrum was double-integrated and the integrated area was compared with that obtained from a known concentration of SDSL ubiquitin. The concentrations were normalized by the concentration at the starting point (t=0), which gave the relative concentrations. Two independent experiments were carried out using oocytes taken from two individual female frogs (Xenopus A and B). The obtained time course data were fitted to a single exponential decay curve, in which least square fitting of the data to the following equation was performed.

$$C = A \cdot \exp(-t/T)$$

where C is relative concentration, A is a constant, and T is the characteristic time constant for decrease in the amount of spin-label radicals. The lines indicate the best fit to the data of the equation. The time constant T was 65.7 ± 3.3 min. The estimated half-life of the intracellular “active” spin labels was approximately 50 min (Figure 3-4).

It should be noted that the starting point, t=0, is at the end of microinjection. Since microinjection to a group of about 50 oocytes usually takes 5-7 min, the incubation period averaged over these oocytes has an uncertainty due to this time lag. Approximately, 30 μM of the nitroxide radicals remained active in the cells even after 2 h of incubation (Figure 3-4).

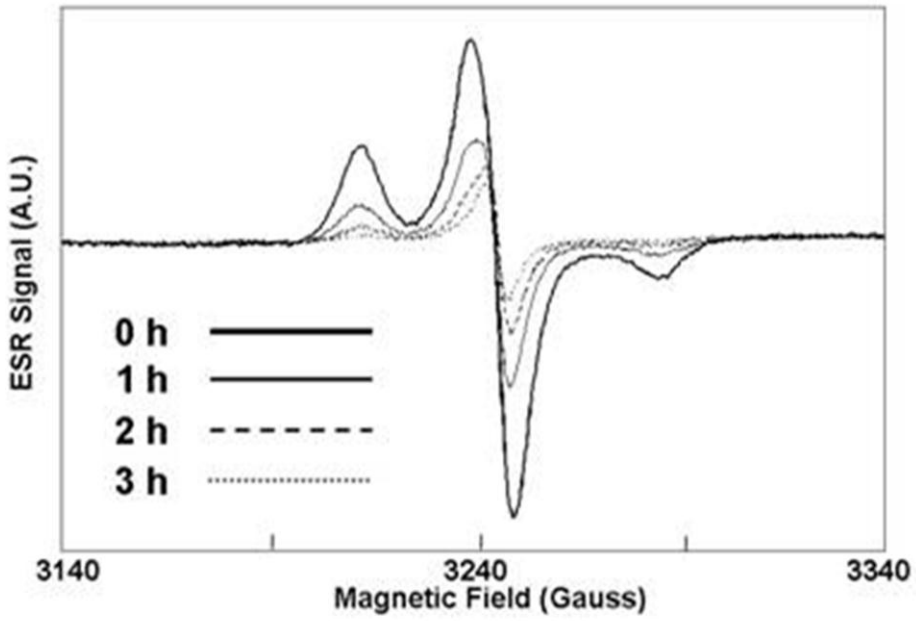

Figure 3-3 Overlay of CW-ESR spectra of S20C-G35C in Xenopus oocytes collected at 0, 1, 2 and 3 hours after injection.

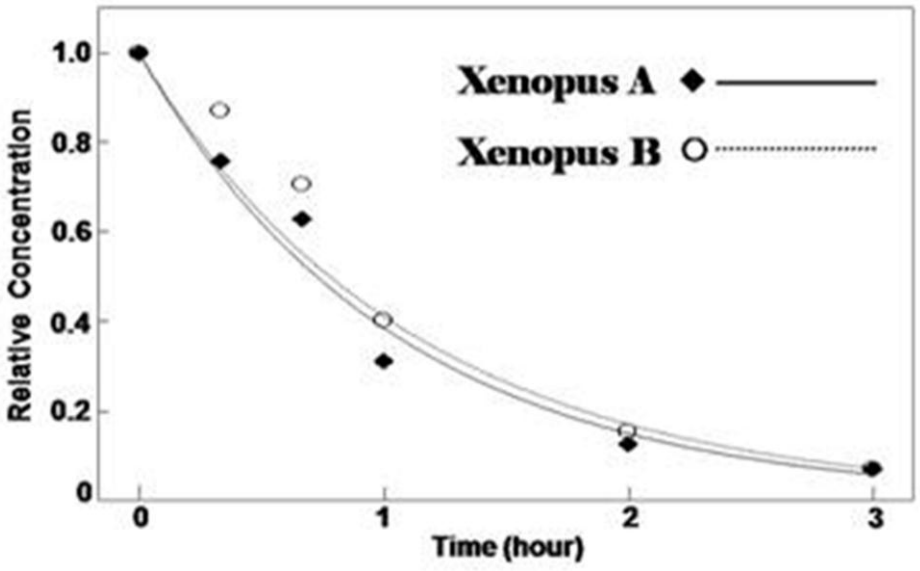

Figure 3-4 The relative concentrations of nitroxide spins plotted as a function of time.

3.3 In-cell DEER Measurements

We then acquired DEER data on oocytes injected with SDSL ubiquitin derivatives.[10] In addition to S20C-G35C, we labeled a ubiquitin derivative with cysteine substitutions at Gly35 and Asp52 (designated G35C-D52C) for the experiments.

Figure 3-5a and 3-5b show dipolar modulation DEER echo curves for spin labeled ubiquitin derivatives both in vivo and in vitro. The interspin distances (r) and their distribution widths (σr, the standard deviation of the distance) were estimated using the single-Gaussian fit method from time domain data after subtraction of the effects of intermolecular dipolar interactions[11,12] (Figure 3-6a, 3-6b, and Table 3-1). The obtained r values were confirmed to be consistent with those extracted by the Tikhonov regularization method[13] implemented in DeerAnalysis2009[12] (Figure 3-7).

Table 1. Inter-spin distances (r) and distance distributions (Δr) in ubiquitin derivatives determined with DEER experiments.

labeled sites		*in vitro*	*in cell* (0 hr)	*in cell* (1 hr)
S20C, G35C	r/nm	3.11 ± 0.05 [a)]	3.14 ± 0.08 [c)]	2.97 ± 0.09 [c)]
	Δr/nm	0.80 ± 0.15 [a)]	1.15 ± 0.13 [c)]	1.37 ± 0.07 [c)]
G35C, D52C	r/nm	2.65 ± 0.06 [b)]	2.60 ± 0.12 [d)]	2.56 ± 0.18 [c)]
	Δr/nm	0.79 ± 0.13 [b)]	1.17 ± 0.20 [d)]	1.57 ± 0.15 [c)]

Experimental errors were estimated from (a) 9, (b) 7, (c) 3 and (d) 4 independent experiments.

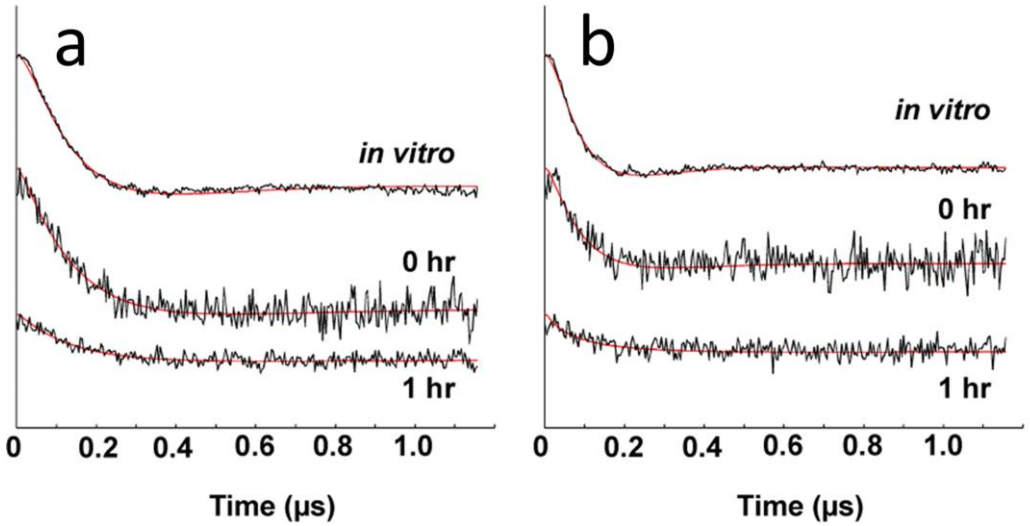

Figure 3-5 Constant-time DEER spectra of S20C-G35C (a) and G35C-D52C (b) ubiquitin in Vitro and in cell (at 0 and 1 h after injection). An exponential decay component due to intermolecular interactions has been subtracted from the spectra. The fits to the data are plotted by the red lines.

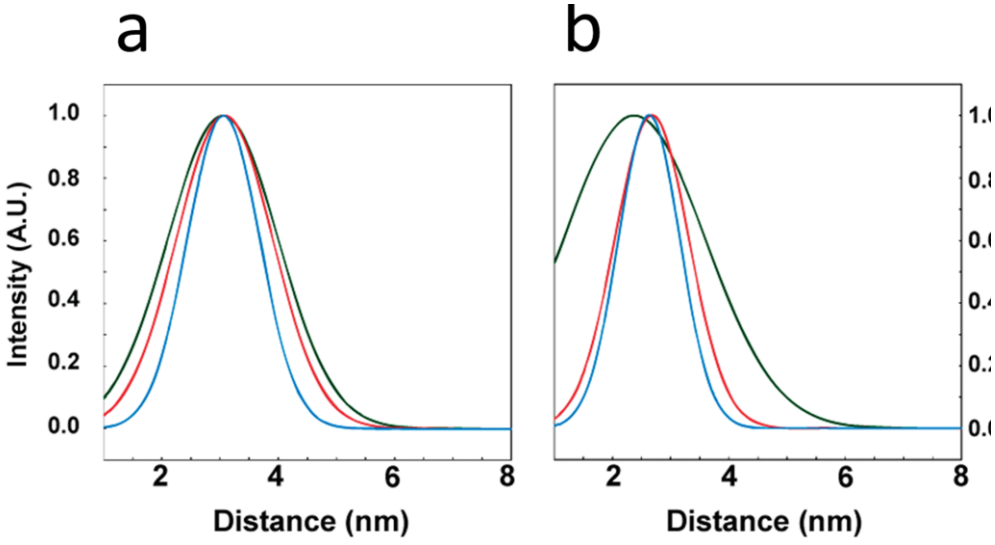

Figure 3-6 Distance profiles of S20C-G35C (a) and G35C-D52C (b) measured in Vitro (blue) and in cells either 0 h (red) or 1 h (green) after injection into cells. The profiles were obtained using the single-Gaussian fit method from time domain data.

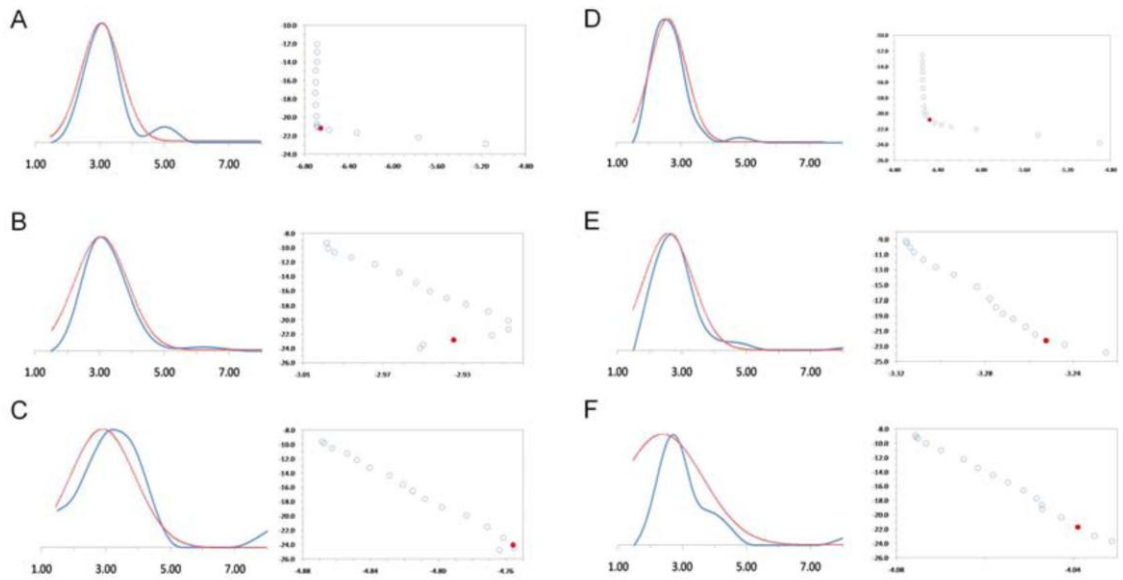

Figure 3-7 Tikhonov regularization (TKR) to obtain distance distribution. A-C. Distance distributions (left) and L-curves (right) for S20C-G35C ubiquitin in vitro and in-cell at 0 and 1 h after injection, respectively. D-F. Distance distributions (left) and L-curves (right) for G35C-D52C ubiquitin in vitro and in-cell at 0 and 1 h after injection, respectively. The red circles in L-curves correspond to the regularization parameter used. The blue and red lines show profiles obtained using TKR and single-Gaussian fit, respectively.

3.4 Results of distance determination in ubiquitin inside Xenopus oocytes

The DEER data in the oocytes gave interspin distances, r, similar to those obtained from the in vitro reference (Figure 3-6a and 3-6b; Table 3-1). The r values of the S20C-G35C and G35C-D52C proteins obtained from the DEER measurements in oocytes were 3.14 and 2.60 nm, respectively, and the in vitro values were 3.11 and 2.65 nm, respectively. This observation suggests that the r values inside the oocytes were similar to those determined in vitro and that the ubiquitin derivatives display no large structural differences between an intracellular and an in vitro environment, which is consistent with our previous observation.[9]

The distance between C_α atoms at the positions of the labeled residues ($R_{\alpha\alpha}$) in S20C-G35C and G35C-D52C was estimated to be 2.3 and 1.8 nm, respectively, from the crystal structure of wild-type ubiquitin (PDB ID: 1UBQ). The differences between their DEER-derived r values in vitro and Rαα, 0.81 and 0.85 nm, respectively, can be attributed to side chain tethering of the nitroxide moiety and the backbone. For methanethiosulfonate (MTSSL)-labeled proteins, the difference between r and $R_{\alpha\alpha}$ was estimated to range from 0 to 1 nm, depending on the conformation of the tethering chain.[1,2] Because the chain length of the 3-maleimido-PROXYL-labeled proteins is longer than that of MTSSL-labeled proteins, the difference between r and $R_{\alpha\alpha}$ could be larger than that of MTSSL-labeled proteins. Thus, we concluded that the deviations of DEER-derived r values in vitro and in cells from Rαα are due to the side chain.

The $\sigma_{<r>}$values in oocytes incubated for 1 h are substantially larger than those without incubation and those from the in vitro reference spectrum. The large $\sigma_{<r>}$ after the 1-h incubation may be due to uncertainty originating from the relatively poor signal-to-noise ratio of the DEER data. The incubation also led to an increase in unpaired spin labels, which may have underscored ESEEM and slightly shortened the obtained r values.

Although $\sigma_{<r>}$ may have a relatively large uncertainty, DEER signals from SDSL proteins incubated in oocytes for 1 h still seem adequate for the estimation of most populated interspin distances. The results suggest that the in-cell pulsed ESR measurements can be applied to studying protein conformational changes that occur within 1 h. With this time window, a variety of biochemical reactions and cellular events are in the scope. For example, stimulation of Xenopus oocytes with progesterone, a steroid hormone, causes a decrease in cAMP levels within minutes, leading to maturation of the oocytes in a few hours. Fertilized eggs of Xenopus laevis develop to Stages 3−4 (4- to 8-cell embryo) in 2 h.[14] Therefore, the pulsed ESR spectroscopy of SDSL proteins in these cells may provide a means to analyze the conformational changes of proteins involved in those cellular and developmental events.

3.5 Conclusion

Although 1H−15N correlation NMR experiments of proteins Xenopus oocytes have been reported,[5,6] *de novo* structural information such as internuclear distances has not been derived from such experiments. In contrast, pulsed ESR is capable of providing long-range distance information on proteins in the intracellular environment, as shown in this study, and thus can complement in-cell NMR.

Microinjection can be implemented on many other cells. However, for in-cell ESR, its applicability is limited to relatively large cells such as the oocytes of zebrafishes, because it requires a large number of spin-labeled proteins. For mammalian cultured cells, one may utilize Cell Penetrating Peptide[7] or other vector systems to deliver SDSL-proteins into the cells, although the lifetime of spin labels may be a critical issue.

In summary, we presented here for the first time SDSL-DEER measurements of proteins in Xenopus oocyte cells. Our data suggest that the method can potentially be used to detect conformational changes of proteins associated with cellular events that occur within 1 h. With this time window, a variety of biochemical reactions and cellular events are within scope.

3.6 Methods

3.6.1 Sample preparation and microinjections

The SDSL ubiquitin derivatives were prepared as described previously[15] with slight modifications. For spin labeling, the proteins were dissolved in 20 mM potassium phosphate buffer (pH 6.8) containing 5 mM KCl and 1 mM EDTA and then incubated overnight at room temperature with a 10 molar excess of 3-maleimido-PROXYL. Unreacted spin-label regents were removed by a desalting column (Sephadex G-25). The gel filtration running buffer was 20 mM potassium phosphate buffer (pH 6.8) containing 5 mM KCl and 1 mM EDTA. Preparation of Xenopus laevis oocytes and microinjection were performed as described previously.[5] Stage V-VI oocytes were selected and used in all experiments. Each oocyte was manually injected with approximately 30 nL of 5 mM spin-labeled protein dissolved in 20 mM potassium phosphate buffer (pH 6.8) containing 5 mM KCl and 1 mM EDTA using a Narishige IM-300 microinjector (Narishige Co. Ltd., Tokyo, Japan). The protein concentration inside the oocyte was estimated to be approximately 150 μM.

For the CW-ESR experiments, the oocytes injected with S20C-G35C ubiquitin were incubated at 18°C for 0, 20, 40, 60, 120 or 180 min. The incubated oocytes were then washed three times with Ca^{2+}-containing MBS buffer (88 mM NaCl, 1.0 mM KCl, 2.4 mM $NaHCO_3$, 0.33 mM $Ca(NO_3)_2$, 0.41 mM $CaCl_2$, 0.82 mM $MgSO_4$, 10 mM HEPES (pH7.6)) that also contained 6% Ficoll (GE Amersham)[5] and then transferred into an ESR tube (5 mm diameter quartz ESR sample tube). The oocytes were settled gently by gravity in the tube. Each sample

contained approximately 50 oocytes. The samples were frozen in liquid nitrogen, and then ESR spectra were measured.

For DEER experiments, oocytes injected with 30 nL of 5 mM S20C-G35C or G35C-D52C ubiquitin were incubated at 18°C for 0 or 60 min. After the incubation period the oocytes were washed and frozen for measurement as described above. Each sample contained approximately 50 oocytes, which occupied about 60 µL in an ESR tube (5 mm diameter quartz ESR sample tube).

3.6.2 ESR measurements

CW-ESR data were acquired at the X-band on a JES-SRE2X spectrometer (JEOL) equipped with an ESR universal cavity (ES-UCX2, JEOL: TE011-mode cavity) and a temperature controller (ES-DVT2, JEOL) using liquid nitrogen at 123 K. The settings for the measurement were as follows: microwave frequency of 9.08 GHz, microwave power of 1.0 mW, time constant of 0.1 s, sweep time of 4 min, center field of 3240 Gauss, sweep width of ±100 Gauss, modulation frequency of 100 kHz, field modulation width of 1 mT and receiver gain of ×40. Each CW-ESR spectrum was double-integrated and the integrated intensity was compared with the intensity of a known concentration of SDSL ubiquitin (150 µM of S20C-G35C-ubiquitin dissolved in 20 mM KPO_4(pH of 6.8), 5 mM KCl and 1 mM EDTA.).

Pulsed DEER data were acquired at 80 K on an ELEXSYS E580 X-band FT/CW spectrometer (Bruker BioSpin) equipped with a dielectric resonator (ER4118X-MD5-W1) and helium gas flow system (CF985, Oxford Instruments). The four-pulse constant-time DEER sequence was employed.[10,15] The pump pulse was set to the maximum of the nitroxide ESR spectrum (ω_B = 9.58 GHz), and the observer pulse was set to 60 MHz higher (ω_A = 9.64 GHz), which corresponds to about a 20 Gauss field separation. These two microwave frequencies (ω_A and ω_B) were supplied by separate microwave sources. The π/2 pulse width was 16 ns, and the durations for π and pump pulses were 32 ns. The acquisition time was set to 1.2 μsec because we did not observe any significant modulation beyond 1 μsec. The total measurement time was chosen depending on the signal-to-noise ratio of the obtained spectra and ranged from 20 to 180 min. The signal contribution of spin-labeled samples that had leaked from the oocytes was assumed to be negligible because the injected oocytes were quickly frozen after extensive washing and were never thawed before the ESR experiments. In order to confirm this assumption, ESR spectra of supernatants that were recovered from gently thaw samples after DEER measurements were acquired and checked.

3.6.3 DEER data analysis

Processing and distance distribution analysis of all time domain DEER signal were performed using the DeerAnalysis2006/2009 program[12] (www.epr.ethz.ch/software/index).

Single-Gaussian-fit was performed to analyze the acquired time traces. An exponential background fitted to the last 3/4 of the time trace was subtracted prior to the fitting. The quality of the fit was also assessed using the software DEFit[11] (http://sites.google.com/site/kadirilkersen/), where multiple-Gaussian-fit can be performed. The assessment showed that a single Gaussian component but no further Gaussian component was adequate for fitting the DEER data. To further verify the distances obtained in this way, the Tikhonov regularization method6 was used to compute the distance distribution functions, where the L-curve criterion was used to find the best regularization parameter (α).

3.6.4 Tikhonov regularization (TKR)

Figure 3-7 shows Tikhonov regularization (TKR) to obtain distance distribution. A-C. Distance distributions (left) and L-curves (right) for S20C-G35C ubiquitin in vitro and in-cell at 0 and 1 h after injection, respectively. D-F. Distance distributions (left) and L-curves (right) for G35C-D52C ubiquitin in vitro and in-cell at 0 and 1 h after injection, respectively. The red circles in L-curves correspond to the regularization parameter used. The blue and red lines show profiles obtained using TKR and single-Gaussian fit, respectively.

For in vitro samples, the L-curve showed a clear inflection and the optimum value was determined as 1000 and 100 for A and D, respectively, which were used to obtain distance distributions (A and D). The distance distributions were reasonably clean with only small long-distance artifacts at around 5 nm, which are presumably due to background correction artifacts as it is generally difficult to estimate a correct background to be subtracted when oscillation of DEER echo curves are not pronounced. Distance profiles obtained using TKR approach are consistent with those obtained with the single-Gaussian fit method.

On the other hand, for in-cell samples, the poorly defined inflection of the L-curve hampered our efforts to find optimum values (B,C,E, and F). This is because the signal-to-noise ratio (SNR) of the DEER data was much lower for the in-cell samples than for in vitro ones. The distance distributions for in-cell samples obtained from the Tikhonov regularization method using value of 10000 are shown in B, C, E, and F. The broadness of the distributions depends on the value used for the regularization as this term represents the balance between smoothness of the distribution function (namely, artifact suppression) and fit to the experimental data. In the case of in-cell data, an optimum that best balanced between the smoothness and the fit was difficult to determine from the L-curve. Thus, value of 10000 was manually selected on the basis of their relatively lower SNR of the time domain data than those of in vitro ones and of a prediction that distance distributions for in-cell samples would not be narrower than those of in vitro ones. The most populated distances obtained in this analysis were consistent with those computed using single-Gaussian fit for all the in vitro and in-cell data.

Reference

1 Borbat, P. P.; McHaourab, H. S.; Freed, J. H. *J. Am. Chem. Soc.* **2002**, 124, 5304–14.

2 Altenbach, C.; Kusnetzow, A. K.; Ernst, O. P.; Hofmann, K. P.; Hubbell, W. L. *Proc. Natl. Acad. Sci. U.S.A.* **2008**, 105, 7439–44.

3 Serber, Z.; Corsini, L.; Durst, F.; Dotsch, V. *Methods Enzymol.* **2005**, 394, 17–41.

4 Li, C.; Charlton, L. M.; Lakkavaram, A.; Seagle, C.; Wang, G.; Young, G. B.; Macdonald, J. M.; Pielak, G. J. *J. Am. Chem. Soc.* **2008**, 130, 6310–1. (c) Burz, D. S.; Dutta, K.; Cowburn, D.; Shekhtman, A. *Nat Methods* **2006**, 3, 91–3.

5 Sakai, T.; Tochio, H.; Tenno, T.; Ito, Y.; Kokubo, T.; Hiroaki, H.; Shirakawa, M. *J. Biomol. NMR* **2006**, 36, 179–88.

6 Selenko, P.; Frueh, D. P.; Elsaesser, S. J.; Haas, W.; Gygi, S. P.; Wagner, G. *Nat. Struct. Mol. Biol.* **2008**, 15, 321–9.

7 Inomata, K.; Ohno, A.; Tochio, H.; Isogai, S.; Tenno, T.; Nakase, I.; Takeuchi, T.; Futaki, S.; Ito, Y.; Hiroaki, H.; Shirakawa, M. *Nature* **2009**, 458, 106–9.

8 Shafer, A. M.; Bennett, V. J.; Kim, P.; Voss, J. C. *J. Biol. Chem.* **2003**, 278, 34203–10.

9 Girvin, M. E.; Fillingame, R. H. *Biochemistry* **1995**, 34, 1635–45.

10 Pannier, M.; Veit, S.; Godt, A.; Jeschke, G.; Spiess, H. W. *J. Magn. Reson.* **2000**, 142, 331–40.

11 Sen, K. I.; Logan, T. M.; Fajer, P. G. *Biochemistry* **2007**, 46, 11639–49.

12 Jeschke, G.; Chechik, V.; Ionita, P.; Godt, A.; Zimmermann, H.; Banham, J.; Timmel, C. R.; Hilger, D.; Jung, H. *Appl. Magn. Reson.* **2006**, 30, 473–98.

13 Chiang, Y. W.; Borbat, P. P.; Freed, J. H. *J. Magn. Reson.* **2005**, 172, 279–95.

14 Ferrell, J. E., Jr. *Bioessays* **1999**, 21, 833–42.

15 Hara, H.; Tenno, T.; Shirakawa, M. *J Magn Reson* **2007**, 184, 78-84.

Chapter 4

Real-time background-free selective imaging of fluorescent nanodiamond *in vivo*

4.1 Introduction

Recent developments of imaging techniques[1] and probes[2,6-8] have enabled fluorescence microscopy to define localization and dynamics of intra-cellular substances of interest even at single-molecular level[9-12]. However, such sensitive detection is often hampered by autofluorescence, arising from endogenous molecules, whose wavelengths are distributed widely and overlapping with those from target fluorescent probes. Such unwanted signals are generally reduced by utilizing differences of either the wavelength or lifetime of the fluorescence; nevertheless, selection of signal of interest is often insufficient, particularly for in-vivo imaging. Here, we develop a novel method for selective imaging of nitrogen-vacancy centers (NVCs) in nanodiamond. The method is based on a unique property that the fluorescence intensity can be modulated by magnetic resonance induced by microwave irradiation. As the NVC fluorescence displays neither photobleaching nor photoblinking owing to extremely high physical and chemical stability, our protocol allows us to conduct long-term tracking of single nanodiamond in *Caenorhabditis elegans* and mouse even in the presence of strong background autofluorescence, with excellent imaging contrast.

NVC is a crystal defect consisting of a nitrogen atom and the adjacent lattice vacancy in diamond[3], and known as a fluorescence-center with good quantum yield of ~1. It also promises stable signal for long period: the fluorescence exhibits neither photobleaching nor blinking[18] unless the diameter of diamond is less than 5 nm[22]. In addition, the wavelength of emitted fluorescence is in the range of 600 nm to 850 nm, which is least absorbed or scattered in biological specimen among visible lights. Unlike quantum dots, the compatibility for living systems is promised by its markedly low

cellular toxicity[20]. Therefore, a few reports of imaging in cells[17-19] and in *C. elegans*[20] have been published to date.

Most prominent feature of NVC is that the electron pairs in NVC emit fluorescence whose intensity depends on the spin states. The pair of electrons form a spin-triplet ($S = 1$), taking two spin energy states of $S_z = 0$ and ± 1 in the absence of static magnetic field. Fluorescence intensities from the electron pair are different by ~20 % between these states. Because of this unique coupling between optical and magnetic properties, NVC attracts a growing interest in the fields of quantum information[13] and nano-scale magnetometry[14,15]. In this paper, we report new fluorescence microscopy for real-time selective observation of nanodiamonds containing NVCs. The method successfully removes autofluorescence of specimen, thus improves effective imaging contrast drastically. We show the method is applicable to a wide variety of living systems from cells to mice.

In this paper, we describe the first real-time background-free selective imaging of FNDs in several classes ranging from HeLa cells to *C. elegans* to mouse with the first report on FND imaging in mouse. We then describe real-time orientation tracking of FNDs in *C. elegans* with ~1° accuracy under the background-free condition.

4.2 Optically detected magnetic resonance (ODMR) based fluorescence modulation of nitrogen-vacancy center (NVC) used for the selective imaging protocol

NVC accommodates one extra electron to form a quantum spin triplet (S = 1) ground state with $^3A_2$ symmetry. Magnetic interaction of the electron with the uniaxial diamond crystal field assigns the 3 electronic spin states of $S_z = +1, 0, -1$ to the $|^3A_2,0\rangle$ and the doubly degenerated $|^3A_2,\pm1\rangle$ sub-levels, respectively. These two sub-levels, separated by ~2.87 GHz (or $\sim10^{-5}$ eV) even in the absence of externally applied magnetic field, are responsible for electron spin resonance (ESR). The spin sub-levels can be read out by ODMR because NVC fluorescence intensity depends on the initial spin sub-levels. On one hand, an electron in $|^3A_2,0\rangle$ is optically pumped to the excited states with ^3E symmetry (by ~2eV above the $^3A_2$ level) and fluorescence is emitted in the decay process en route back to the original $|^3A_2,0\rangle$. On the other hand, an electron in $|^3A_2,\pm1\rangle$ is optically pumped to the same excited states but decays either of two paths (left and right paths in Figure 4-1) with nearly the same probability: one path is back to the original $|^3A_2,\pm1\rangle$ state with fluorescence emission (left), whereas another path passes the $|^3A_2,0\rangle$ state through an non-radiative intermediate meta-stable spin singlet state $|^1A_1,0\rangle$ ($^3E \rightarrow {}^1A_1 \rightarrow {}^3A_2$) with no fluorescence emission (right).

Interestingly, the occupation probability of the initial spin state at $|^3A_2,\pm1\rangle$ can be increased by ESR with microwave (MW) irradiation at the resonant frequency of near 2.87GHz in the absence of externally applied magnetic field, which in turn decreases the NVC fluorescence intensity (see Figure 4-4). Therefore, a repeated process of MW irradiation switching between turned-on and -off under a continuous 532 nm

excitation altered the NVC fluorescence intensity between low and high accordingly (see Figure 4-7c), which was used for the selective imaging in this study.

In the selective imaging protocol, the fluorescence signal only from FNDs could be selectively extracted as shown in Figure 4-7b by a computational routine through subtraction between successive two fluorescence images in the absence and presence of MW irradiation. The decrease of NVC fluorescence intensity by MW irradiation was typically just a few percent of the original fluorescence intensity and thus raw fluorescence images were averaged to obtain high S/N images.

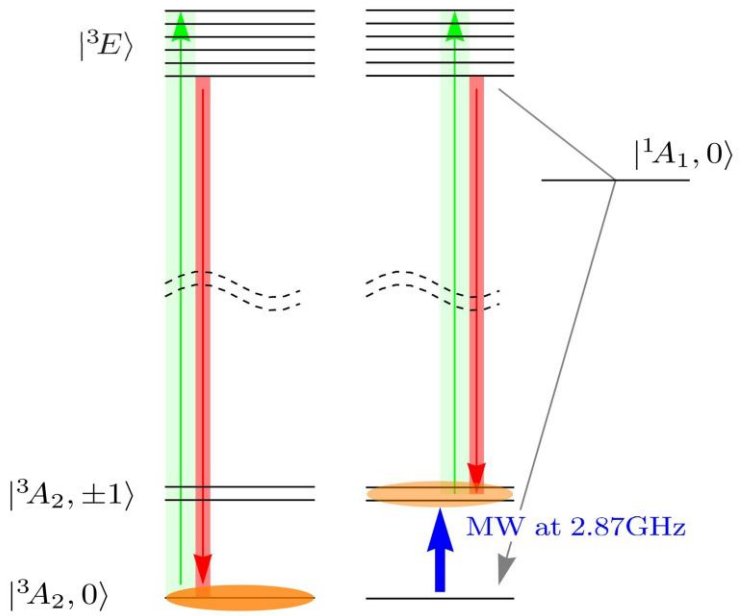

Figure 4-1 Schematic diagram of the electronic energy levels of NVC and the decay processes that can be modulated by electron spin resonance (ESR).

4.3 Simultaneous acquisition of ODMR spectra of multiple FNDs with EMCCD camera

To developed a procedure for selective observation of NVC, we first constructed a microscope for ODMR. Figure 4-2 shows the experimental set-up based on an inverted fluorescence microscope equipped with MW irradiation system to manipulate the occupation of the spin energy levels. We used electron-multiplying charge-coupled device (EMCCD) camera for the photon detection. The EMCCD detects multiple nanodiamonds in the field of view simultaneously, which is methodologically impossible in confocal microscopy due to its raster scanning mechanism[17-19]. Figure 4-3 shows a conventional fluorescence image of NVCs of nanodiamonds dispersed on a coverslip, and 4-4 the ODMR spectra of NVCs in multiple nanodiamonds obtained simultaneously by measuring their fluorescence intensities while sweeping the MW frequency. The fluorescence intensity decreases at 2.87GHz, which implies that the spin state is altered by magnetic resonance, thus the solid proof of resonant phenomenon observed through optical detection. The splitting of dip is caused by a lower distortion of lattice from the original uniaxial crystal field[4,26].

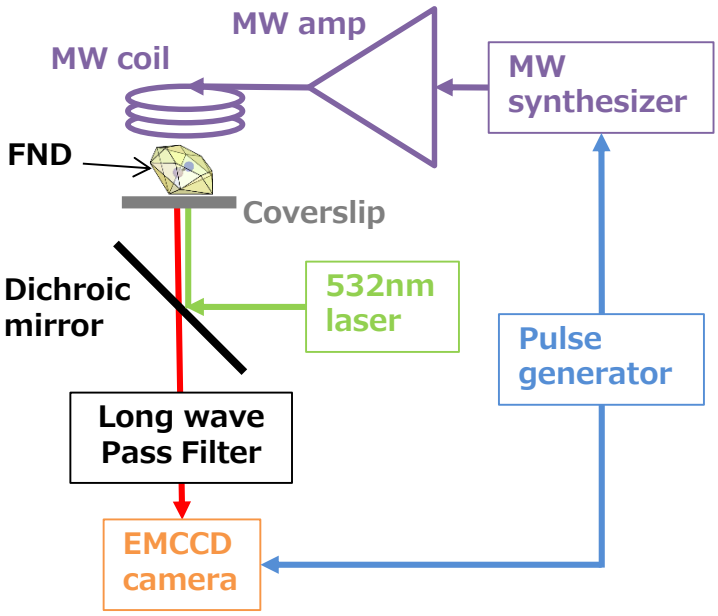

Figure 4-2 Schematic diagram of the experimental set-up. A three-turns copper coil to apply microwave (MW) was placed just above the sample plane on an inverted microscope for ODMR measurements. A continuous wave Nd:YAG laser (λ = 532 nm) used to excite NVCs in FNDs was incident on the sample plane by epi-fluorescence microscopy. The fluorescence from FNDs was passed through a long wavelength pass filter and imaged by an EMCCD camera.

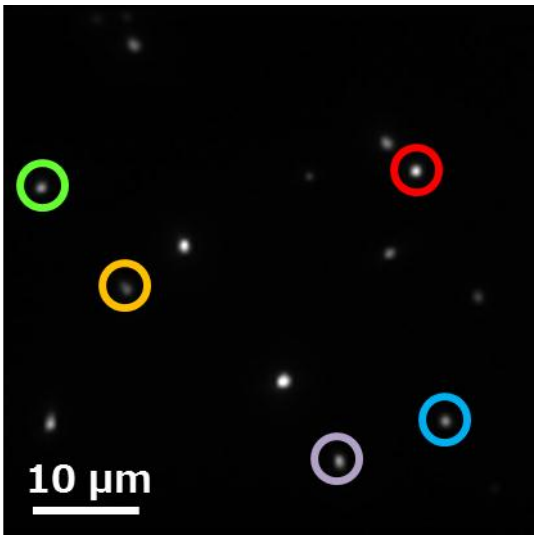

Figure 4-3 Fluorescence image of FNDs in MilliQ water adsorbed on a coverslip (an average of 32 consecutive images, EMCCD exposure = 5 ms).

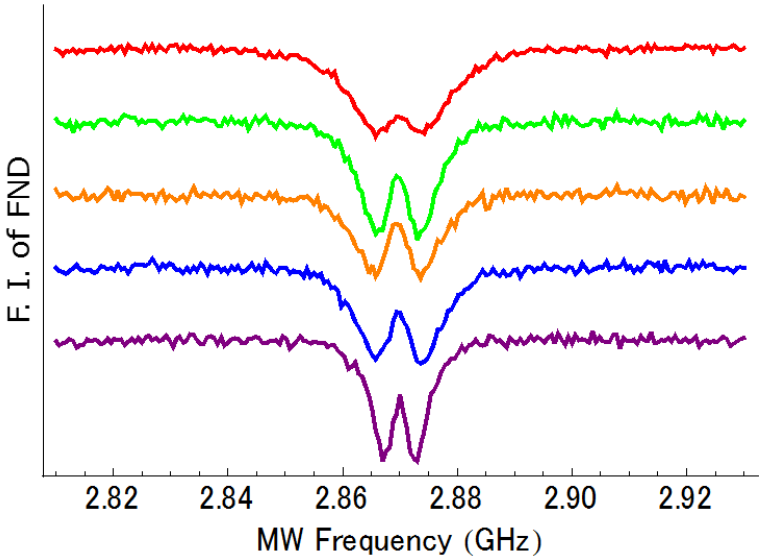

Figure 4-4 ODMR spectra (0.6 MHz resolution, an average of 32 consecutive spectra, EMCCD exposure = 5 ms) of 5 FNDs indicated by the circles in Figure 4-3.

4.4 Capability of single NVC imaging with our setup

To estimate the sensitivity of the microscopy, we measured ODMR spectra of a feeble fluorescence spot at various static magnetic fields. We made sure by ODMR measurements under externally applied magnetic fields that our experimental set-up is able to be used for single NVC imaging. We observed a single pair of dips in ODMR spectra that did not split by higher external magnetic field for several FNDs approximately 50 nm in diameter (Figure 4-5b), indicating that the spot is attributed to single NVC with the probability of 3/4.[4,19,26] We found that another spot with a similar intensity generated the same spectral pattern of two dips (data not shown). The observed NVCs were able to be selectively imaged. When FNDs each contain multiple NVCs, 2–4 pairs of dips are supposed to be observed with a few exceptional cases since multiple NVCs possibly point toward different directions among 4 possible orientations. The two exceptional cases in which a pair of dips can be observed for multiple NVCs are (i) The angle between the NVCs and the external magnetic field coincides with the magic angle of 54.7°and (ii) All the NVCs point toward the same orientation among possible 4 orientations.

We can exclude the first case by our ODMR measurements. The magic angle (θ = 54.7°), a half of the angle between NVC axes (109.47°) is the angle which produces a single pair of dips in ODMR spectra even for NVCs pointing towards the maximum of 4 different orientations. Figure 4-5 shows MW frequency of a pair of dips observed from an FND under 6 external magnetic field with different magnitudes (0, 0.9, 2.6, 3.4, 5.8, and 9.8 mT) and simulated MW frequency curves of the dips for several angle conditions. The observed data is not fitted with the magic angle θ = 54.7° but fitted well with an

angle $\theta = 71.5°$, indicating that NVC(s) in the FND pointed toward a single orientation in the FND.

With respect to second case, unfortunately, we cannot exclude its possibility by our ODMR measurements, however, we are convinced that our set-up is able to be used for imaging single NVCs since the estimated fluorescence from a single NVC is sufficient to be detected with EMCCD. The product of the molar extinction coefficient of NVC at 532 nm, $(8.1 \pm 2.1) \times 10^3$ $M^{-1}cm^{-1}$ calculated from a published absorption cross section[27], and the quantum yield of NVC[4] (≈ 1) is comparable with that of Cy3 (molar extinction coefficient at 532 nm = 85,600 $M^{-1}cm^{-1}$, quantum yield = 0.15), the most popular dye used in single-molecule fluorescence imaging. In fact, average fluorescence intensity of 3 FNDs which were estimated to contain single NVCs from ODMR spectra was approximately one tenth of that of 6 quantum dots (Qdot655) excited by the same laser intensity, which agrees well that Cy3 emits ~1/10 fluorescence of a quantum dot. Moreover, the probability of n NVCs with a unidirectional orientation in an FND is $4^{-(n-1)}$ which rapidly decreases with the increase of the number of NVC. In the worst scenario where several NVC(s) had been imaged, still single NVC fluorescence signal obtained by dividing the observed fluorescence by n was high enough to be imaged. Thus, together with the above discussion we conclude that our set-up has single NVC imaging capability. For more direct proof of single NVC imaging should be obtained by a photon correlation measurement[19].

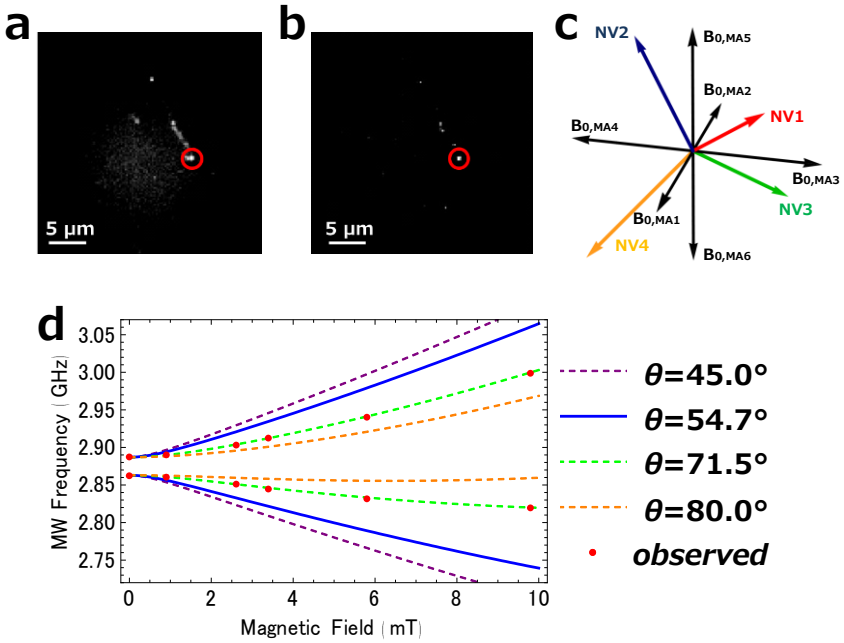

Figure 4-5 a,b, Fluorescence images of FNDs on a coverslip without (a) and with (b) selective imaging protocol. The fluorescent spot indicated by a red circle is an FND containing of single NVC. a,b are created by the same procedure for Figure 2b,c from 32 consecutive images (EMCCD exposure = 50 ms). **c,** Schematic drawing of the possible four orientations of a NVC in FND and our definition of angles (θ, φ) between a NVC orientation and the externally applied magnetic field H0. **d,** MW frequency of a pair of dips observed from an FND (red points) under 6 external magnetic field with different magnitudes (0, 0.9, 2.6, 3.4, 5.8, and 9.8 mT) and MW frequency simulated for several angle conditions.

4.5 Selective imaging of FND on a coverslip and inside HeLa cells

By using the property that the fluorescence intensity of NVC, but not of other sources, changes upon the resonant MW irradiation at 2.87GHz, we developed a method of selective imaging protocol (SIP) of NVCs. Figure 4-6 shows the time chart employed in the protocol for gated MW irradiation and synchronized image acquisition by EMCCD. The alternative irradiation generates a modulation in fluorescence intensity of NVC due to its unique fluorescence property (see supplementary information for more details), whereas non-NVC fluorescences are not affected by MW thus having the constant intensity, as schematically illustrated in the lower two panels of Figure 4-6. The image acquisition synchronized with MW switched on and off and the subsequent image processing (subtraction in the paired images) should leave finite intensity for the fluorescence from NVCs but minimal in other regions. This expected behavior was clearly observed in time courses of fluorescence intensity as shown in Figure 4-7(a) for nanodiamonds and fluorescent beads spread over a coverslip, and the consequent selective image 4-7(c) taken in such a way exhibits only nanodiamond signals.

SIP can dissolve a fluorescence spot originated from plural nanodiamonds that reside within an optical resolution. The ODMR spectrum of a single fluorescence spot under static magnetic field shown in Figure 4-8 reveals that the spot consists of two nanodiamonds whose crystal lattices orient differently to each other. Choosing appropriate MW irradiation frequencies, we could selectively visualize each nanodiamond by SIP, pseudo-logically extending optical diffraction limit.

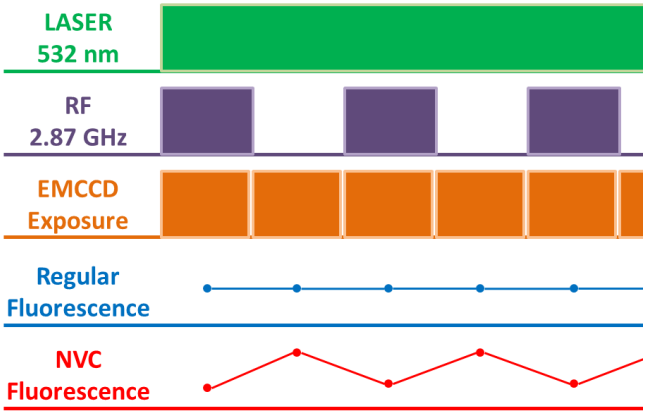

Figure 4-6 Time chart of 532 nm excitation, MW irradiation and image acquisition used for selective imaging protocol, and expected fluorescence profiles of non-NVC and NVC.

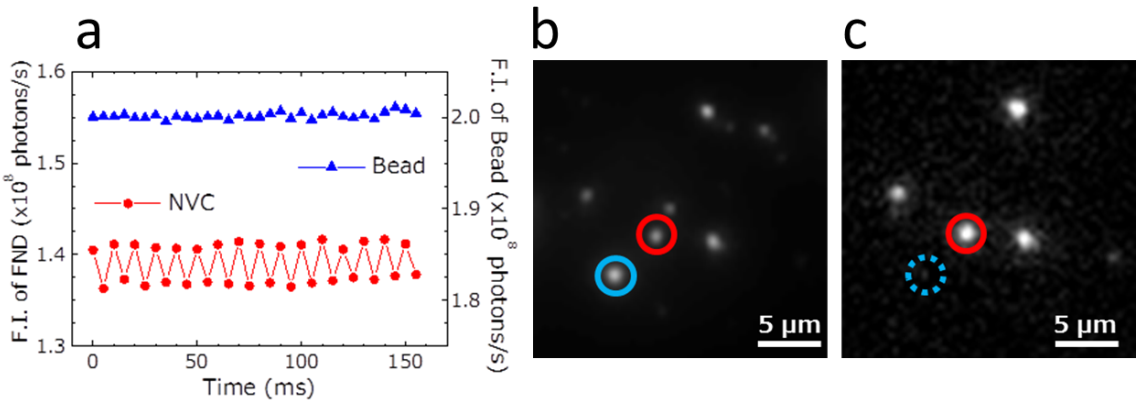

Figure 4-7 (a) Time courses of fluorescence intensity of the FND indicated by the red circle and the fluorescent bead indicated by the blue circle in (c). (c), (d) Fluorescence images of FNDs (red) and fluorescent microspheres 0.11 μm in diameter (blue) adsorbed on a coverslip (c) without selective imaging protocol and (d) with selective imaging protocol. c,d are created from the same 32 consecutive images (EMCCD exposure = 5 ms) consisting of 16 pairs of 2 consecutive images, an image with MW irradiation and the subsequent image without MW irradiation. c is an average of the 32 images, whereas d is an average of 16 images each of which is created by the subtraction between the 2 images of a pair, subtraction of an image with MW irradiation from the subsequent image without MW irradiation.

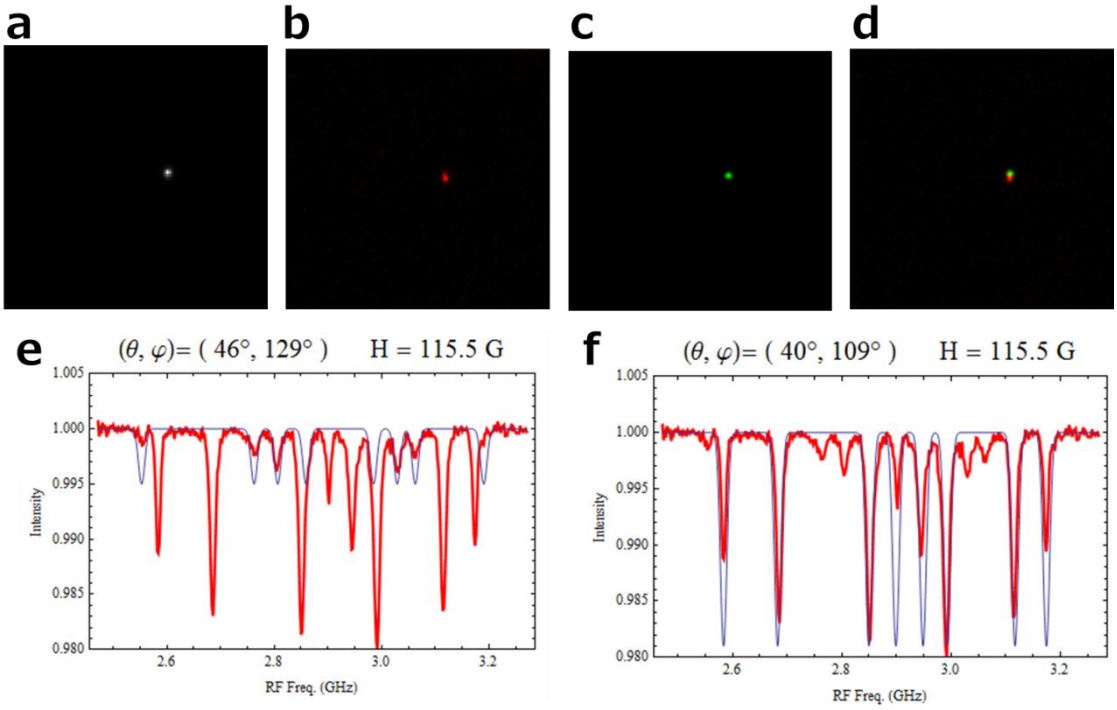

Figure 4-8 (a) Fluorescent image of FNDs without selective imaging protocol. (b), (c) With selective imaging protocol using microwave frequency of 2804 MHz and 2850 MHz respectively. (d) Merged image of (b) and (c). (e), (f) ODMR spectrum (4.0 MHz resolution, an average of 16 spectra, EMCCD exposure = 10 ms) of the FNDs.

The performance of SIP was first demonstrated for living HeLa cell containing both nanodiamonds and fluorescent beads for mimicking strong background signals. In contrast to the conventional fluorescence image (Figure 4-9(b)), the image in Figure 4-9(c) taken with SIP clearly displays only the fluorescence of NVC and total absence of those from fluorescence beads with markedly high contrast. Owing to the absence of photo-bleaching of NVCs, the quality of the images exhibited no time-dependent degradation. Thus method offers continuous real-time observation as long as cells are alive on the microscope stage (see supplementary movie). Regarding the time resolution, the accumulated exposure time of ~160 ms (equivalent to the frame rate) was enough to produce the high-quality selective image of nanodiamonds with diameter ~200 nm and a few hundreds of NVCs contained (assuming NVC density 10^{-7}/carbon). In order to estimate a frame rate of SIP imaging for single NVC, we analyzed the correlation between signal intensity and the noise profile (see Supplemental Information). Assuming 5 % decrease of fluorescence at the resonance condition, the frame rate of 27 ms is required to obtain signal-to-noise ratio equal to unity for the SIP image. It should be noted that ODMR spectra of single NVCs in HeLa cell measured by using confocal microscopy were recently reported.

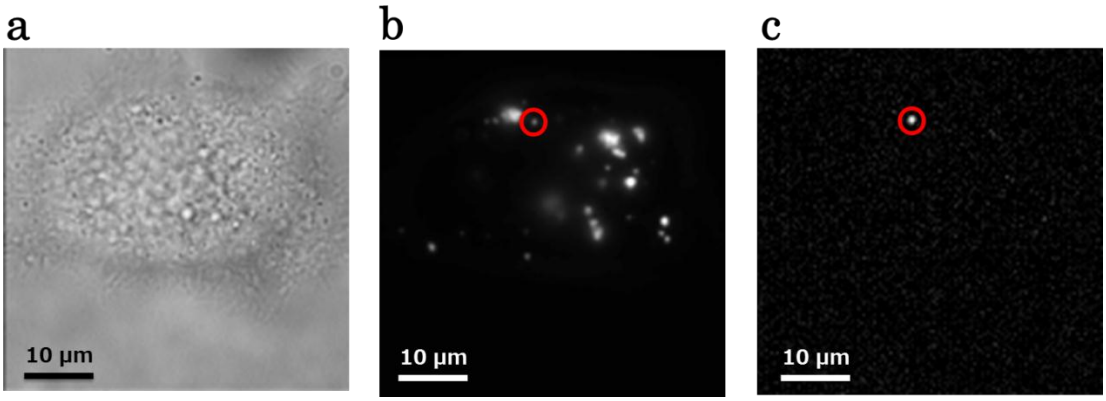

Figure 4-9 (a)-(c), Selective imaging of an FND inside HeLa cells. (a), Bright-field image.(b), Fluorescence image without selective imaging protocol. (c), Fluorescence image with selective imaging protocol. (b), (c) are created by the same procedure for 4-7 from the same 128 consecutive images (EMCCD exposure = 2.5 ms) .

4.6 Selective imaging of an FND inside *C. elegans*

The feasibility of in vivo SIP was examined in Caenorhabditis elegans. As shown in the whole-body image taken by the conventional fluorescence method (Figure 4-10(a)), autofluorescences are present throughout the body and markedly intense in intestine. These autofluorescences prevent us from identifying the signals from NVCs (Figure 4-10(d)-(e)). However, in vivo SIP clearly removed these background signals and allowed us to selectively detect the signals from NVCs localized in the intestinal lumen. Further evidence that the extracted signal certainly originates from NVCs in nanodiamond was given by measuring the ODMR spectrum on the remaining fluorescence (g), which reveals the characteristic decrease of fluorescence at 2.87 GHz (h). In vivo SIP also identifies the signal from NVC incorporated into intracellular region of intestine. These experiments demonstrate that the SIP is powerful in obtaining high quality selective image of nanodiamond probes at highly noisy background.

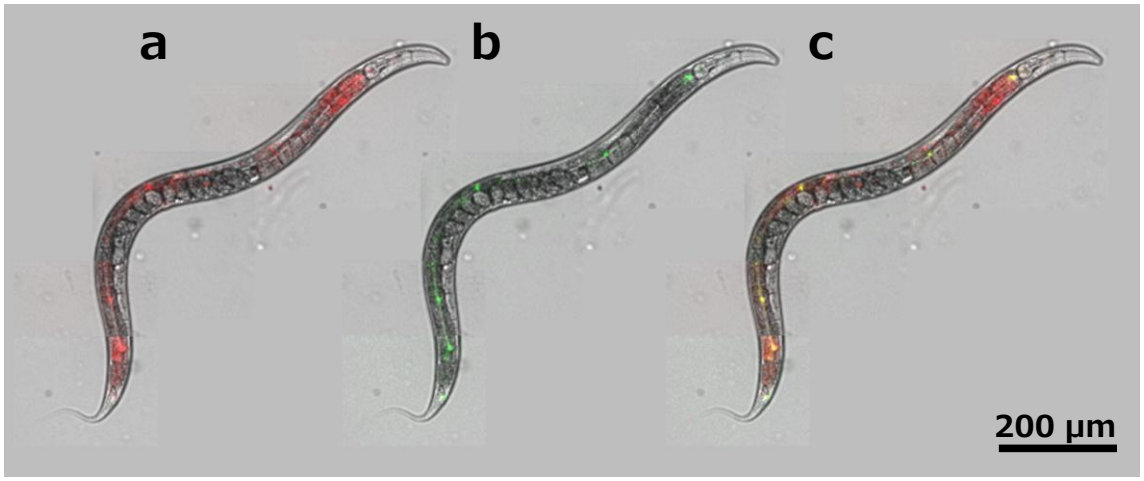

Figure 4-10 (a)-(c) Bright-field/fluorescence merged images of a living wild-type *C. elegans* fed with FNDs. (a) Without selective imaging protocol. Red represents overall fluorescence. (b) With selective imaging protocol. Green represents selectively imaged FND fluorescence. (c) Merged image of (a) and (b). Red and yellow indicate autofluorescence and FNDs selectively imaged, respectively. Fluorescence images of (b), (c) are created by the same procedure for Figure 4-7 from 32 consecutive images (EMCCD exposure = 33 ms)

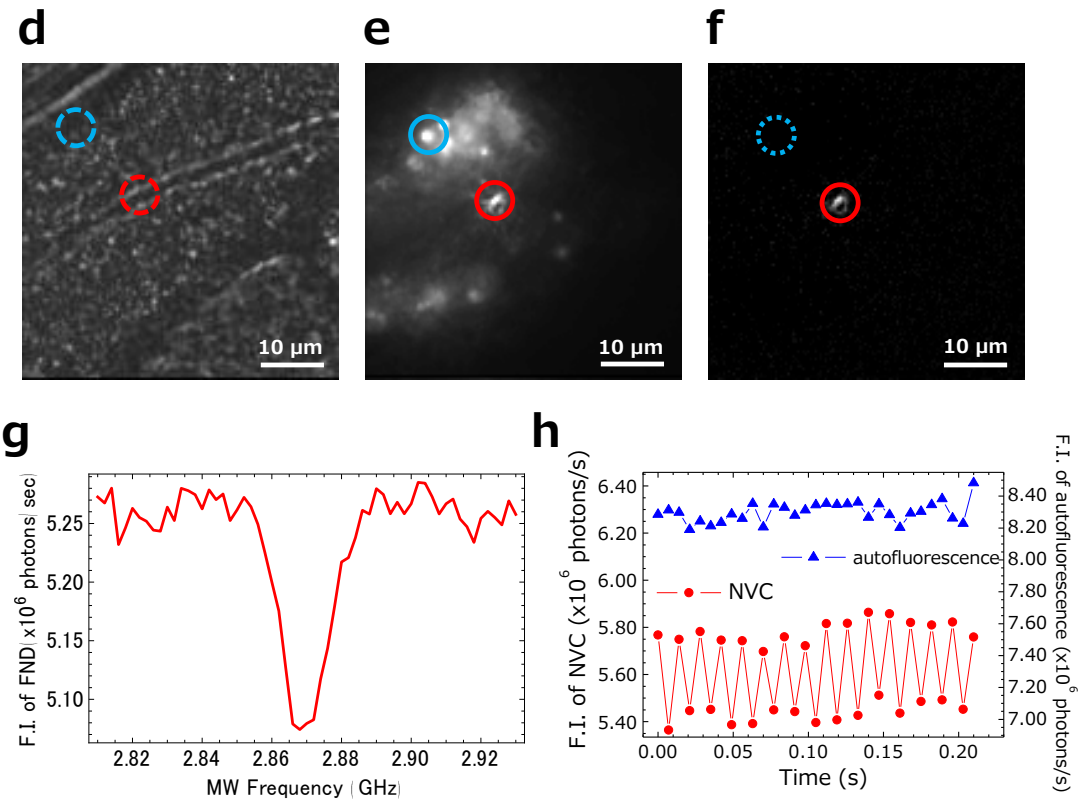

(d) Bright-field image of the intestine of *C. elegans*. Red and blue circles indicate the positions of an FND in the intestine and autofluorescence, respectively. (e), (f) Fluorescence images (e) without selective imaging protocol and (f) with selective imaging protocol. (e), (f) are created by the same procedure for Figure 4-7 from 32 consecutive images (EMCCD exposure = 7 ms). (g), ODMR spectrum (2.0 MHz resolution, an average of 16 spectra, EMCCD exposure = 10 ms) of the FND indicated by a red circle in (e), (f). (h) Time courses of fluorescence intensity for an FND indicated by red circle and autofluorescence indicated blue circle in (e), (f).

4.7 Selective imaging of an FND aggregate inside a nude mouse

SIP is also applicable to mice. We injected nanodiamonds into a region of intraperitoneal of a nude mouse with the depths in the range of 400~500 μm (Figure 4-11(a)). Whereas strong fluorescence from endogenous substances was observed and indistinguishable from those of NVCs in the conventional image (Figure 4-11(b)), the background signals are completely erased and only those from the injected nanodiamonds were visualized in the SIP image (Figure 4-11(c)). The quality of ODMR spectra from nanodiamonds was invariant at least for an hour, indicating that continuous real-time imaging is possible for the duration. The viability of mouse monitored by its respiration, showed no noticeable change during the period of observation, indicating the low invasiveness of the method as was also observed in the experiments using *C.elegans*. Noteworthy, the SIP performance is not perturbed by fluctuations of fluorescence intensities caused by respiration, because the sampling rate for SIP is much faster than the respiration cycle (red line in Figure 4-11(b)).

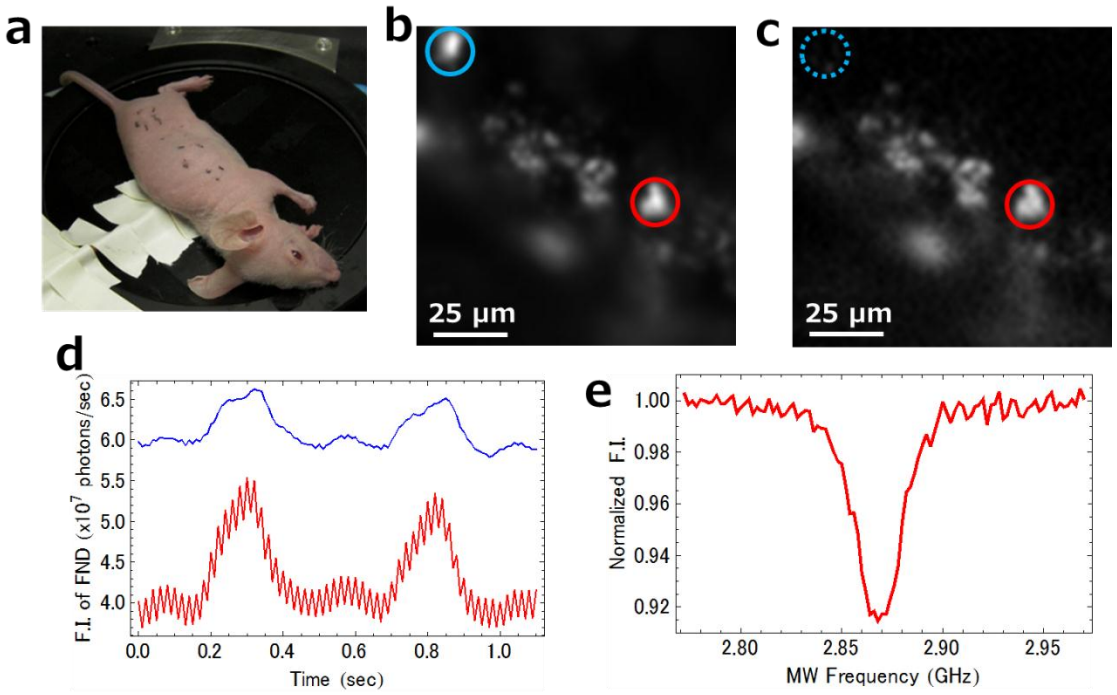

Figure 4-11 Photograph of the nude mouse used in this experiment lying on the sample plane. The MW coil was taped to be fixed on the sample plane and to avoid direct contact with the mouse. (b), (c), Fluorescence images (b) without selective imaging protocol and (c) with selective imaging protocol. (b), (c) are created by the same procedure for Figure 4-7b, c from 32 consecutive images (EMCCD exposure = 10 ms). Red and blue circles indicate an FND aggregate located in intradermal tissue and autofluorescence, respectively. (d) Time courses of fluorescence intensity for FNDs indicated by red circle and autofluorescence indicated blue circle in (b), (c). (e) ODMR spectrum (2.0 MHz resolution, an average of 32 spectra, EMCCD exposure = 10 ms) of the FND indicated by a red circle in (b), (c).

4.8 Orientation tracking of an FND in the intestine of *C. elegans*

We then observed rotational dynamics of FNDs in the intestine of *C. elegans* by extending the selective imaging protocol. We tracked rotational dynamics of selectively observed FNDs in living wild-type, dead wild-type, and living *itr-1 (sa73)* mutated *C. elegans* to examined how the intestinal activity reflects the dynamics. *itr-1(sa73)* is a gene that encodes an inositol trisphosphate (IP_3) receptor, a protein that controls muscle contraction by regulating intracellular calcium levels. It is known that IP_3 receptor is critical to the Ca^{2+} regulation in the intestinal epidermal cells and thus the mutation severely impairs the intestinal activity. Rotational dynamics of FND containing single NVC in living HeLa cells has been recently reported[19], where an angle between the externally applied magnetic field and the NV axis was monitored. However, the measurement could not determine another rotational angle perpendicular to the magnetic field. Here, to determine the orientation of an FND defined by two rotational angles (θ, φ) to the external static magnetic field $\mathbf{H_0}$ as shown in Figure 4-12a, we used relatively large FNDs several hundreds of nanometers in diameter each of which contained several tens of NVCs. Figure 4-12c shows four ODMR spectra (red) under an external static magnetic field ($\mathbf{H_0}$ = 6.6 mT) and the best fitted curve (blue), showing that our extended protocol allows to determine both of the two angles with ~1° accuracy. Orientation determination of single nanometer-sized probes has been achieved by measuring the fluorescence polarization anisotropy[9,11,29] or polarization-dependent absorption[30] either of which is based on anisotropic optical properties of the probes. However, the angular precision of the measurements is ~10° at best. As shown in Figure

4-12d, the angular trajectory in the living wild-type *C.elegans* (red) exhibited the highest intestine activity evidenced by the FND rolling movement with an average angular velocity of ~1°/min, whereas the trajectory in the dead wild-type *C.elegans* (blue) suggests inactivity of the intestine represented by the localized angular trajectory. Interestingly, the magnitude of the rolling movement in the living mutant was much smaller than that in the living wild-type, which is consistent with a past observation that the *itr-1 (sa73)* mutant exhibits slower defecation cycle than the wild-type[5]. This experiment is a proof-of-principle experiment demonstrating that ODMR measurement offers a tool to quantitatively monitor subtle physiological activities *in vivo*.

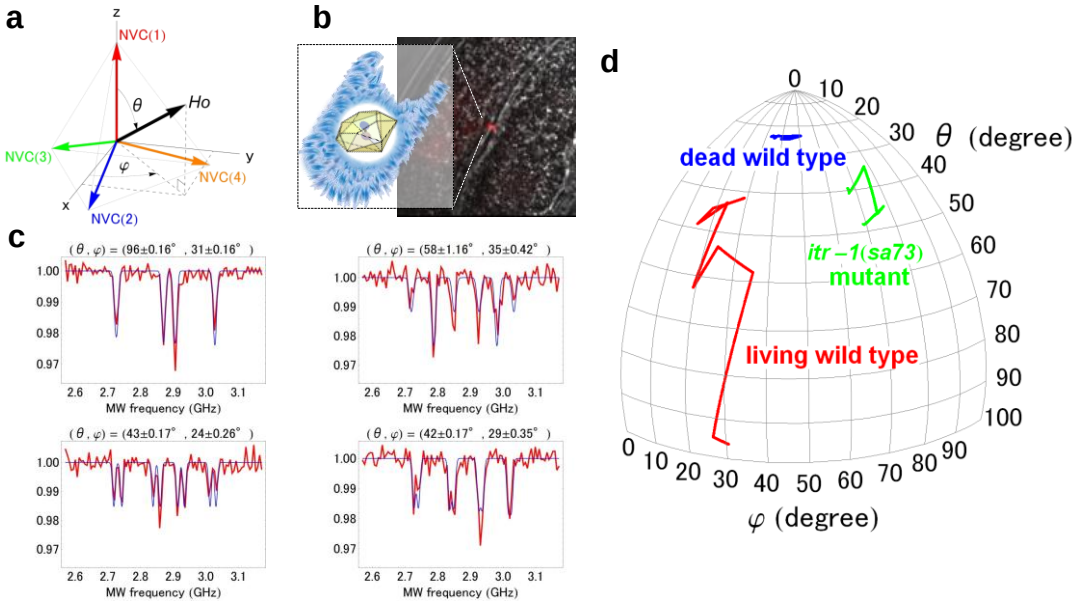

Figure 4-12 (a), Schematic drawing of the possible 4 orientations of a NVC (NVC (1)~(4)) in FND and our definition of rotational angles (θ, φ) between a NVC orientation (NVC (1)) and the externally applied magnetic field H_0. Each NVC principal axis coincides with the nitrogen-vacancy bonding in the diamond crystal. The orientation of NVC(1) is defined as the z-axis in a Cartesian coordinate system, rendering the orientation of NVC (2) expressed by a unit vector of $(\sin\alpha,\ 0, \cos\alpha)$ where α = 109.47°. The orientations of the NVC (3) and NVC (4) are determined in the same manner. (b), Bright-field/fluorescence merged image (an average of consecutive 32 images with MW irradiation, EMCCD exposure = 10 ms) and schematic drawing of an FND in the intestine of *C. elegans*. (c), Typical ODMR spectra (red, 6 MHz resolution, an average of 16 spectra, EMCCD exposure = 10 ms) of an FND in living wild-type *C. elegans* under external static magnetic field (H_0 = 6.6 mT) and the best fitted curves (blue). (d), Angular trajectories (time resolution ~30 s) of FNDs located on the intestine inner wall of a living wild-type (red), a dead wild-type (blue) and a living *itr-1 (sa73)* mutant (green).

4.9 Conclusion

In this paper, we describe a method for real time selective fluorescence imaging of diamond NVCs, which does not rely on either difference of wavelength of excitation or emission light or fluorescence life time. Recently selective imaging was also proposed for nitrospirobenzopyran derivative which can be photo-chemically converted from fluorescence inactive to active forms by near-ultraviolet irradiation[6,23]. Although they performed lock-in detection, the time resolution is an order of several seconds because the spontaneous conversion from fluorescence active to inactive forms is slow at room temperature. In addition, damages caused by irradiation at 365 nm might not be negligible for living cells and organisms, which may largely limit its biological applications. Therefore, advantages of our method may contain the time resolution and durations for real-time tracking. Video-rate continuous imaging is possible for hours without any decrease in the intensities of signals, owing to extremely high physical and chemical properties of nanodiamonds. In addition, the invasiveness caused by optical and microwave irradiations seem to be minute: During the experiments shown here, no noticeable deteriorating effect was observed for the viabilities of cells, nematodes and mouse (data).

NVC-containing nanodiamonds are expected to be one of most promising fluorescence probes, which can be tagged to various biomacromolecules, organelle, cells and viruses. The method to produce homogeneous nanodiamonds with the diameters of 5 nm, comparable with the size of GFP fluorescence protein, has been reported, which are both fluorescence and magnetic resonance- positive. Several protocols have been proposed to chemically modify the surfaces of Nanodiamonds, so that they can be

conjugated to other molecules. Thus it is possible to label biomolecules and cellular components with 5 nm diamonds. Our SIP would be most powerful in tracking nanodiamond-tagged molecules in cells and *in vivo*, to localize them and to analyze their dynamic properties. NVC diamond has several advantages as a fluorescence probe: The fluorescence efficiency is almost equivalent to that of Cy3 and Qdot, and the cellular toxicity has been shown to be markedly low in clear contrasts with quantum dots[25,26]. With those remarkable properties and SIP demonstrated here, it would be possible for the first time to track the motion of molecule continuously in time period from milliseconds to hours in cells or organisms.

4.10 Methods

4.10.1 Experimental set-up

Experiments were performed on an inverted microscope (ECLIPSE Ti, Nikon) with a three-turns copper coil (diameter, ~1 mm) placed just above the sample plane to apply MW for ODMR. A continuous-wave Nd:YAG laser (Compass 315-M, Coherent) used to excite NVCs at 532 nm was incident on the sample plane by epi-fluorescence microscopy. The incident light intensity was 2 mW for imaging an FND inside *C. elegans*, 4 mW for imaging FNDs on a coverslip, and 6 mW for imaging FND inside HeLa cells and a mouse. The illuminated area was 1.3×10^3 μm^2, thus the excitation density was 1.5, 3.1, and 4.6×10^2 W/cm^2, respectively. The fluorescence from NVCs was collected by either an oil immersion 60× objective (ApoTIRF, NA = 1.49, Nikon) or a 10×

objective (PlanFluor ×10, NA = 0.30, Nikon), passed through a dichroic mirror (DM575: Nikon) and a long wavelength pass filter (BLP01-635R-25, Semrock) to eliminate the excitation light, and imaged by an EMCCD camera (DU-860, Andor Technology). MW generated by a MW synthesizer (E8257D, Agilent) was amplified by a linear MW power amp with 45 dB gain (ZHL-16W-43+, Minicircuit), and then transmitted to a three-turns copper coil (~1 mm in diameter) placed just above the sample plane. To obtain ODMR images, triggers were sent to a pulse generator (model 565, Berkeley Nucleonics Corporation) to generate periodic TTL signals to synchronize MW irradiation switching and EMCCD exposure. The MW frequency was 2.87 GHz for the selective imaging of FNDs, whereas the frequency was swept for ODMR spectra acquisition as indicated.

4.10.2 FND preparation

We prepared FNDs by crushing irradiated synthetic type Ib single-crystal diamonds because they have better crystallinity and lower background luminescence emission than synthetic diamond powders produced by detonation techniques or natural diamond powders. Type Ib single-crystal diamonds were synthesized by a temperature-gradient method under a high-pressure and high-temperature (HPHT) condition (5.5 GPa, 1,350 °C) in which an iron-alloy system was used as a solvent and a high-purity carbon source. Nitrogen concentration of the synthetic diamonds was estimated by FT-IR spectroscopy to be about 100 ppm on average. The synthetic

diamonds were irradiated with a 4.6 MeV electron beam up to a dose of 100 kGy and annealed at 800 °C for 1 h *in vacuo*. The irradiation and annealing treatment created NVCs in the diamonds, which were seen as a color change of the diamonds from yellow to red and detectable as a clear peak at 637 nm in Raman spectroscopy. Next, the treated diamonds were powdered by crushing with stainless steel balls in a milling jar and then washed by an acid treatment to remove any metal contaminants of the balls and the jar. Finally, the powdered diamonds were dissolved in a mixture of acetone and ethanol, which separated FNDs as a supernatant by precipitating large, micrometer-scale diamonds. FNDs used in the experiments were obtained by evaporation of the supernatant solvent.

4.10.3 Sample preparation for imaging FNDs on a coverslip

We used FND solution obtained as a supernatant of pre-dissolved 10 μg/ml FND solution in MilliQ water in which relatively large FNDs spontaneously precipitated. The diameter of the FNDs was a few hundred nanometers. In the experiments shown in Figure 4-2, we dropped 10 μl of the supernatant onto a coverslip and imaged FNDs in the supernatant that were non-specifically adsorbed on the surface after washing out unbound FNDs with 100μl of MilliQ water. In the experiments shown in Figure 4-8 in which fluorescent beads were present, we dropped 10 μl of the supernatant and 10 μl of 0.002% (v/v) fluorescent bead (F-8801, 0.11 μm in diameter, red fluorescent (580/605), Molecular Probes) suspension in MilliQ onto a coverslip and

mixed by a micropipette on it. We imaged FNDs and fluorescent beads in the mixture that were non-specifically adsorbed on the surface after washing out unbound FNDs and fluoresecent beads with 100μl of MilliQ water.

4.10.4 HeLa cell preparation

HeLa cells were cultured on a 50-mm tissue culture dish with a cover glass bottom (World Precision Instruments) for 24 hours in 2 ml of Dulbecco's modified Eagle's medium (DMEM, #12430, Invitrogen) supplemented with 10% (v/v) fetal bovine serum (FBS, #10437, Invitrogen) and 1% (v/v) peniillin/streptomycin (#15140, Invitrogen). To introduce FNDs and the fluorescent beads into the cells, we added a mixture containing 10 μl of 10 μg/ml FND in DMEM and 10 μl of the 0.002% (v/v) fluorescent bead suspension in MilliQ to the outside of the cover glass bottom area of the dish and incubated overnight at 37°C in a 5% CO_2 atmosphere. To remove extracellular FNDs, fluorescent bead, and phenol red in the medium, we washed the dish three times with 2 ml of phenol red-free DMEM (#21063, Invitrogen) supplemented with the same amount of FBS and the antibiotics. The cells were subjected to the measurement at 37°C on a temperature controlled plate (MATS-55RAF20, TOKAI HIT) after addition of 2 mL of phenol red-free DMEM to the dish. The diameter of the FNDs imaged inside the cells was several hundred nanometers.

4.10.5 *C. elegans* preparation

The wild-type N2 Bristol strain and *itr-1(sa73)* mutant used in this study were maintained and handled by standard methods, and prepared as follows. Firstly, the worms were grown to an adult stage at 20°C on a nematode growth medium (NGM) plate seeded with *E. coli* (OP50) bacteria as a food source. Secondly, 10 ml of ~1 mg/ml FND suspension in MilliQ was added onto the 5 mm-diameter lawn of the *E. coli* to feed FNDs to the worms. Thirdly, 10 adult worms were transferred to a new FND-seeded NGM plate and incubated at 20°C for 3 h to recover from the crowded condition. Finally, worms were glued onto a 1.5% agar pad formed on a coverslip, immersed in M9 buffer, sandwiched with a coverslip, and subject to the measurements. The diameter of the FNDs imaged inside the cells was several hundred nanometers.

4.10.6 Nude mouse preparation

A female 7-week-old *BALB/cAJcl-nu/nu* mouse (CLEA) was anesthetized with 50 mg/kg of sodium pentobarbital (Abot) by intraperitoneal injection. Then the mouse was given a single intradermal injection of 100 µl of 100 µg/ml FND suspended in PBS using a microsyringe (Hamilton) equipped with a 30G needle (Termo). The diameter of the FNDs imaged inside the cells was several hundred nanometers. This animal experiment was approved by the Animal Research Committee of Kyoto University and

carried out in strict accordance with the guidelines for animal experiments from the committee.

4.10.7 Determination of rotational angles of FNDs

The obtained ODMR spectra were analyzed based on the diagonalization of Hamiltonian composed of zero-field terms and a magnetic Zeeman term as described below.

$$H = D\left\{S_z^2 - \frac{1}{3}S(S+1)\right\} + E\left(S_x^2 - S_y^2\right) + \gamma_e \mathbf{H_0} \cdot \mathbf{S} \quad (1)$$

where D and E are zero-field splitting parameters, $\boldsymbol{S}$ is the electronic spin with the magnitude of unity, Sx, Sy and Sz are the spin components, γ_e and $\mathbf{H_0}$ are the electronic gyromagnetic ratio and the externally applied magnetic field, respectively. Since FNDs used in this study (several hundred nanometers in diameter) contained as many as several tens of NVCs, their orientations were presumably distributed among the 4 equivalent <111> axes with equal probability (25%). Actually, 8 dips consisting of 4 pairs of 2 dips in measured ODMR spectra were well fitted with simulated spectra based on the equal probability assumption, providing relative changes of the two angles (θ, φ) between FNDs and $\mathbf{H_0}$.

To obtain the rotational angles (θ, φ), we performed the non-linear least-square fit of ODMR spectra with the Hamiltonian expressed in equation (1). The fit provided

angles with a certain residual minimum as well as 4 fitting parameters, D, **Ho**, the width of gaussian kernel for convolution, and the amplitude of fluorescence intensity. However, there must be a couple of best fitted angles due to the C_{3v} crystal symmetry of 4 NVC axes. To show how we determined the angles, we draw the distribution maps of the residues obtained by the fit. The residues are obtained by calculating the square of difference between the fitting and observed spectra where the angles (θ, φ) were explicitly specified while the rest of 4 parameters remained constant.

Figure 4-13a displays a series of the maps for 9 spectra of the wild-type *C.elegans*. As seen in the maps, there are a couple of best fitted angles with nearly the same residue, all of which provide undistinguishable theoretical spectra. In this study, we set a criterion to select one of the best fitted angles: we selected the angles nearest from the selected angles in the previous map. The red circle indicates the angles (θ, φ) we selected for presenting in Figure4-12d.

The same procedure is adopted for the determination of (θ, φ) for the dead wild-type *C.elegans* and *itr-1 (sa73)* mutant. Their distribution maps of residues are shown in Figure4-13b,c. In contrast to the wild-type living *C.elegans*, little or smaller change is seen in the maps for the dead wild-type *C.elegans* and *itr-1 (sa73)* mutant, respectively.

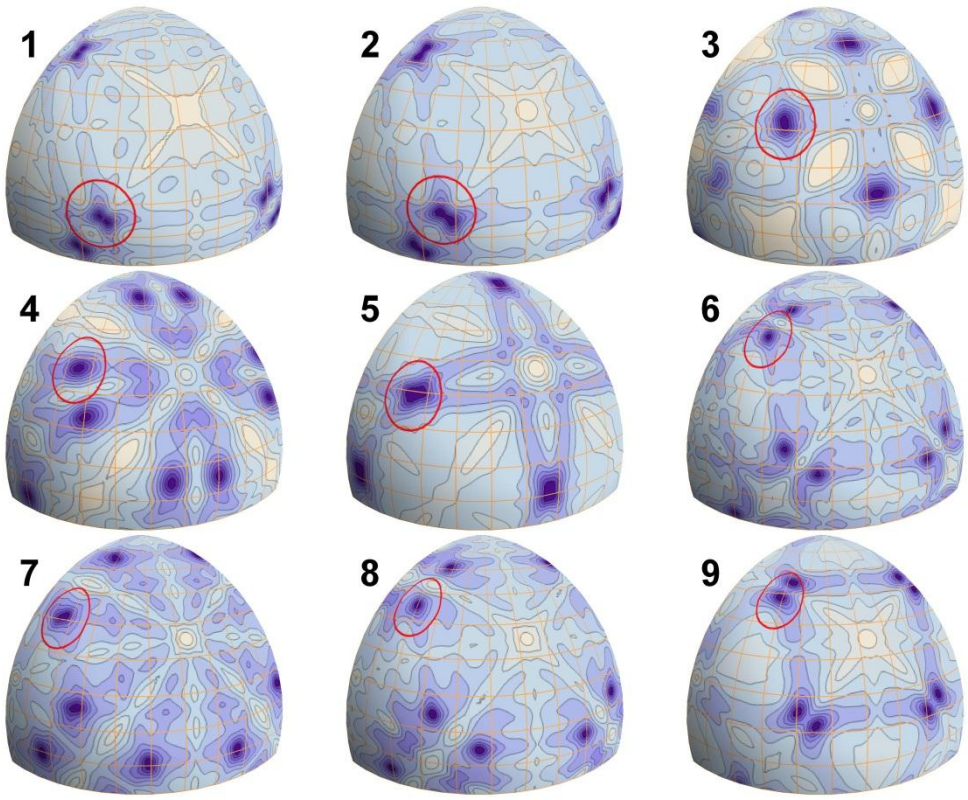

Figure 4-13a One-quarter hemispherical density maps of the residue in the non-linear least-square fit of the rotational angles (θ, φ) of an FND inside living wild-type *C. elegans*. Red circles indicate the angles determined in dark regions with smaller residues where the angles were best fitted. The numbers located at top left of the plots indicate the chronological order.

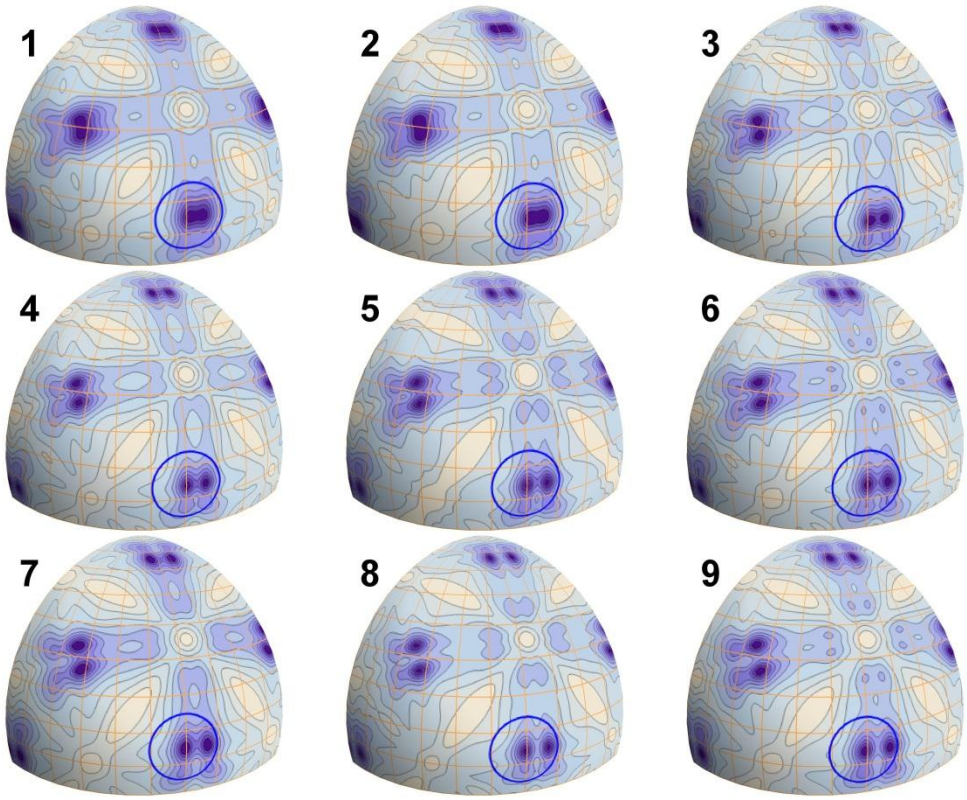

Figure 4-13b One-quarter hemispherical density maps of the residue in the non-linear least-square fit of the rotational angles (θ, φ) of an FND inside dead wild-type *C. elegans*.

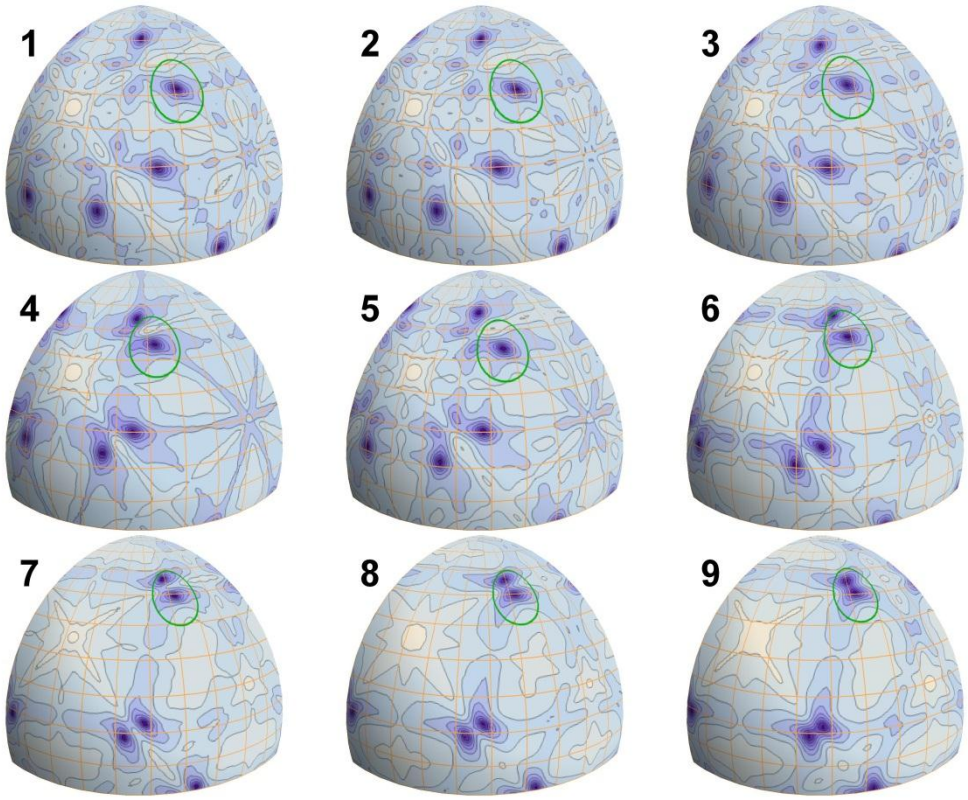

Figure 4-13c One-quarter hemispherical density maps of the residue in the non-linear least-square fit of the rotational angles (θ, φ) of an FND inside living *itr-1 (sa73)* mutant.

Reference

1 Huang, B., Babcock, H. & Zhuang, X. Breaking the diffraction barrier: super-resolution imaging of cells. *Cell* **2010**, 143, 1047-1058

2 Giepmans, B. N., Adams, S. R., Ellisman, M. H. & Tsien, R. Y. The fluorescent toolbox for assessing protein location and function. *Science* **2006**, 312, 217-224 (2006).

3 Aharonovich, I., Greentree, A. D. & Prawer, S. Diamond photonics. *Nature Photon.* **2011**, 5, 397-405 .

4 Gruber, A. et al. Scanning confocal optical microscopy and magnetic resonance on single defect centers. *Science* **1997**, 276, 2012-2014.

5 Dal Santo, P., Logan, M. A., Chisholm, A. D. & Jorgensen, E. M. The inositol trisphosphate receptor regulates a 50-second behavioral rhythm in C. elegans. *Cell* **1999**, 98, 757-767 .

6 Shaner, N. C., Steinbach, P. A. & Tsien, R. Y. A guide to choosing fluorescent proteins. *Nat. Methods* **2005**, 2, 905-909.

7 Marriott, G. et al. Optical lock-in detection imaging microscopy for contrast-enhanced imaging in living cells. *Proc. Natl. Acad. Sci. USA* **2008**, 105, 17789-17794.

8 Grotjohann, T. et al. Diffraction-unlimited all-optical imaging and writing with a photochromic GFP. *Nature* **2011**, 478, 204-208.

9 Toprak, E. & Selvin, P. R. New fluorescent tools for watching nanometer-scale conformational changes of single molecules. *Annu. Rev. Biophys. Biomol. Struct.* **2007**, 36, 349-369.

10 Joo, C., Balci, H., Ishitsuka, Y., Buranachai, C. & Ha, T. Advances in single-molecule fluorescence methods for molecular biology. *Annu. Rev. Biochem.* **2008**, 77, 51-76.

11 Beausang, J. F., Schroeder 3rd, H. W., Nelson, P. C. & Goldman, Y. E. Twirling of actin by myosins II and V observed via polarized TIRF in a modified gliding assay. *Biophys. J.* **2008**, 95, 5820–5831.

12 Lord, S. J., Lee, H. L. & Moerner, W. E. Single-molecule spectroscopy and imaging of biomolecules in living cells. *Anal. Chem.* **2010**, 82, 2192-2203.

13 Dutt, M. V. G. et al. Quantum register based on individual electronic and nuclear spin qubits in diamond. *Science* **2007**, 316, 1312-1316.

14 Balasubramanian, G. et al. Nanoscale imaging magnetometry with diamond spins under ambient conditions. *Nature* **2008**, 455, 648-651.

15 Grinolds, M. S. et al. Quantum control of proximal spins using nanoscale magnetic resonance imaging. *Nature Phys.* **2011**, 7, 687-692

16 Ho, D. Beyond the sparkle: the impact of nanodiamonds as biolabeling and therapeutic agents. *ACS Nano* **2009**, 3, 3825-3829.

17 Chang, H. C. et al. Mass production and dynamic imaging of fluorescent

nanodiamonds. *Nature Nanotech.* **2008**, 3, 284-288.

18 Faklaris, O. et al. Comparison of the photoluminescence properties of semiconductor quantum dots and non-blinking diamond nanoparticles. Observation of the diffusion of diamond nanoparticles in living cells. *J. Eur. Opt. Soc. Rapid. Publ.* **2009**, 4, 09035.

19 McGuinness, L. P. et al. Quantum measurement and orientation tracking of fluorescent nanodiamonds inside living cells. *Nature Nanotech.* **2011**, 6, 358-363.

20 Mohan, N., Chen, C.-S., Hsieh, H.-H., Wu, Y.-C. & Chang, H.-C. In vivo imaging and toxicity assessments of fluorescent nanodiamonds in Caenorhabditis elegans. *Nano Lett.* **2010**, 10, 3692–3699.

21 Chang, I. P. et al. Facile surface functionalization of nanodiamonds. *Langmuir* **2010**, 26, 3685-3689.

22 Bradac, C. et al. Observation and control of blinking nitrogen-vacancy centres in discrete nanodiamonds. *Nature Nanotech.* **2010**, 5, 345-349.

23 Jobsis, F. F. Noninvasive, infrared monitoring of cerebral and myocardial oxygen sufficiency and circulatory parameters. *Science* **1977**, 198, 1264-1267.

24 Ntziachristos, V. Going deeper than microscopy: the optical imaging frontier in biology. *Nat. Methods* **2010**, 7, 603-614.

25 Hall, L. T. et al. Monitoring ion-channel function in real time through quantum decoherence. *Proc. Natl. Acad. Sci. USA* **2010**, 107, 18777-18782.

26 Batalov, A. et al. Low temperature studies of the excited-state structure of negatively charged nitrogen-vacancy color centers in diamond. *Phys. Rev. Lett.* **2009**, 102, 195506.

27 Wee, T. L. et al. Two-photon excited fluorescence of nitrogen-vacancy centers in proton-irradiated type ib diamond. *J. Phys. Chem. A* **2007** 111, 9379-9386.

28 The C. elegans Sequencing Consortium. Genome sequence of the nematode C. elegans: a platform for investigating biology. *Science* **1998**, 282, 2012-2018 .

29 Chung, I., Shimizu, K. T. & Bawendi, M. G. Room temperature measurements of the 3D orientation of single CdSe quantum dots using polarization microscopy. *Proc. Natl. Acad. Sci. USA* **2003**, 100, 405-408.

30 Xiao, L., Qiao, Y., He, Y. & Yeung, E. S. Three dimensional orientational imaging of nanoparticles with darkfield microscopy. *Anal. Chem.* **2010**, 82, 5268-5274

Chapter 5

General conclusion

General conclusion

Suppression of the background noise is not perfect in double resonance experiments but becomes satisfactory using a triple resonance technique for selective detection of metabolism. Importantly, the present ^{1}H probe is a novel “switch-on” type, which is otherwise NMR-silent and is rendered active only when transformed into the target metabolite by the metabolic reaction in concern. The method thus allows simple and unambiguous detection of specific metabolic event without requiring laborious and possibly misleading chemical shift analysis of the probe and its various metabolites. The present strategy is also applicable to other NMR-active (I = 1/2) nuclei, such as ^{15}N. Since sequences such as H-C-C and H-C-N are common in biorelevant molecules, there are plenty of potential candidate molecules as biomarkers that can be detected using the present technique. In principle, this approach can be applied directly for in vivo MRI/MRS through the spatially dependency of gradient magnetic field.

SDSL-DEER is capable of providing *De novo* structural information such as internuclear long-range distances on proteins in the intracellular environment, as shown in this study, and thus can complement in-cell NMR. Potentially, the method can be used to detect conformational changes of proteins associated with cellular events that occur within 1 h. With this time window, a variety of biochemical reactions and cellular events are within scope. Microinjection can be implemented on many other cells. However, for in-cell ESR, its applicability is limited to relatively large cells such as the oocytes of zebrafishes, because it requires a large number of spin-labeled proteins. For mammalian cultured cells, one may utilize some vector systems to deliver SDSL-proteins into the cells, although the lifetime of spin labels may be a critical issue.

The results confirm in chapter 4 the feasibility of the ODMR selective imaging of FNDs in biological targets ranging from living cells to multicellular organisms to higher animals. The results confirm that ODMR with an externally applied magnetic field allows us to perform real-time background-free orientation determination of FNDs inside multicellular organisms with ~1° accuracy. This microscopy will be widely applicable to real-time live cell, organism, and animal imaging in which high background, mainly autofluorescence, degrades image quality. Furthermore, with the flexible labeling capability and non-toxicity of FNDs, this new microscopy can be used for investigating *in vivo* subtle motions of target biomolecules that have not been observed under nearly no background conditions.

We can use the higher polarization of ^{1}H spin for monitoring metabolism of ^{13}C-labeled biomolecules. We can use the higher polarization of electron spin for internuclear distance determination on intracellular proteins. We can use optical polarized electron spin instead of the usual thermal Boltzmann polarization for MR cellular imaging. In conclusion, this work reveals the utility of selective detection of the highly polarized spin using MR methods, triple resonance NMR, SDSL-DEER and ODMR selective imaging of FNDs, for biological measurement *ex vivo*, in cell and *in vivo*.